Patrik Aspermair, BSc.

Odorant sensing with functionalized graphene field-effect transistors utilizing impedance spectroscopy

MASTER'S THESIS

to achieve the university degree of

Master of Science

Master's degree programme: Biomedical Engineering

submitted to

Graz University of Technology

Supervisor

Ao.Univ.-Prof. Dipl.-Ing. Dr.techn. Hermann Scharfetter

Institute of Medical Engineering

Prof. Dr. Wolfgang Knoll
AIT Vienna

Graz, Februar 2016

This work was funded by the Austrian Institute of Technology, Vienna.

AFFIDAVIT

I declare that I have authored this thesis independently, that I have not used other than the declared sources/resources, and that I have explicitly indicated all material which has been quoted either literally or by content from the sources used. The text document uploaded to TUGRAZonline is identical to the present master's thesis dissertation.

date	(signature)

0.1 Abstract

The label-free detection of odorant biomolecules on bases of electrochemical devices is the first step towards an artificial nose. In this work the unique electrochemical properties of graphene are utilized to create a biosensing platform for the detection of odorants, using surface-immobilized odorant binding proteins.

Herein, the suitability of impedance spectroscopy applied to reduced graphene oxide based field-effect transistors for detection of biological binding events is demonstrated. The impedance Z as a function of the analyte bulk concentration in aqueous solution was measured. The immobilized odorant binding proteins influence the charge carriers in the channel of the graphene field-effect transistor (gFET) significantly, changing the impedance Z during the binding of specific analytes. Negative control measurements of the analyte without immobilized odorant binding proteins have been performed to validate the specificity of the biosensor. Furthermore, the dependencies to pH values and ionic concentrations of the aqueous solutions are shown. Different protective layers on the graphene surface were applied to reduce the unspecific responses. The Langmuir isotherm was used to determine the affinity of ligands to odorant binding proteins and the advantages of impedance spectroscopy measurements on the graphene field-effect transistor are discussed for further investigations.

0.2 Kurzfassung

Die markierungsfreie Detektion von odorant Biomolekülen auf Basis eines elektrochemischen Gerätes ist der erste Schritt in Richtung einer künstlichen Nase. In dieser Arbeit werden die einzigartigen elechtrochemischen Eigenschaften von Graphen genutzt, um eine biosensorische Umgebung für die Detektion von Odoranten mit immobilisierten odorant-bindenden Proteinen zu schaffen.

Die Eignung von Impedanzspektroskopie, angewendet an Feldeffekttransistoren, basierend auf reduziertem Graphenoxid für die Detektion von biologischen Bindeereignissen, wird im folgenden gezeigt. Die elektrische Impedanz Z wurde als Funktion der Analytenkonzentration in wässriger Lösung gemessen. Die immobilisierten odorant-bindenden Proteine beeinflussen die Ladungsträger im Kanal des Feldeffekttransistors signifikant, was zur Änderung der Impedanz Z während der spezifischen Analytenanbindung führt. Es wurden ebenfalls Negativkontrollen bei gleichem Analyten aber ohne immobilisierten odorant-bindenden Proteinen durchgeführt, wodurch die Spezifität des Biosensors überprüft wurde. Außerdem werden die Abhängigkeiten von pH-Wertänderungen und Änderungen der Ionenkonzentrationen der wässrigen Lösung gezeigt. Es wurden unterschiedliche Schutzschichten auf die Grapheneoberfläche aufgebracht um die unspezifischen Bindungen zu reduzieren. Das Modell der Langmuir Isotherme wurde verwendet um die Affinitäten der Liganden zum odorant-bindenden Protein festzustellen. Die Vorteile der impedanzspektroskopischen Messungen am Graphen Feldeffekttransistor werden für weitere Untersuchungen diskutiert.

Contents

1 Introduction

Since the discovery of graphene in 2004, the carbon nanomaterial has drawn much attention from the scientific world, due to its unique properties. Numerous reports and studies concerning this two-dimensional crystal have been carried out to investigate its fundamental mechanical, electrical and optical properties and it remains a field of growing interest. Nowadays it is possible to produce large flake size graphene at a large scale and hence new industrial applications are being thought of i.e. replacement of current industrial materials and the creation of new devices.

But what is graphene? Graphene is a mono layer of carbon atoms, arranged in a hexagonal pattern, with only one atom of structural height. The characteristic shape is often compared to a honeycomb and forms a network of aromatic-like carbon hexagons. In general, graphene is considered as an infinitely large aromatic area. Beside its mechanical and thermal applications it became very interesting in the studies of biosensors, graphene has been studied especially in the field of biosensors for its unique electrical properties. Graphene plays an outstanding role in electronics as a highly conducting material, with semi-metallic properties. The thickness of just one atomic layer forms an almost transparent material with a transmittance of 97.7% at $\lambda = 550$ nm [1], making it to an invisible conductor. The biocompatibility of carbon, combined with electrical conductivity forms a transducer module for biological events to be converted to electrical signals. This gives graphene a boost in biosensor technologies and creates new possibilities for the detection of specific molecules at the nano scale, leading to high sensitivities, low limits of detection and good specificity. Electric fields, such as created in field-effect transistors, can be applied to enhance the signals of biorecognition events.

In food and drug delivery, biosensors are crucial to detect toxins, impurities, bacteria, viruses or other biological contaminates in a short time with precise results. Nowadays, probes are sent to laboratories to investigate those undesired compounds, raising costs for production controls. A lab-on-a-chip could be a fast solution for those tests, saving time and money. Graphene biosensors are an encouraging new field, worth further investigations. They have the potential

to supplement expensive and bulky optical measurements, such as surface plasmon resonance (SPR) or maybe even replace it.

The development of a field-effect transistor (FET), enhancing the signals for biological binding events with an applied electric field is an approach of a lab-on-a-chip, with just a few components and short assay times. Graphene based FET, also called gFETs, combined with surface immobilized biorecognition molecules, such as antibodies, enzymes or proteins enable the detection of analytes within minutes or even seconds. The transducer's layer being only 1-atom thick allows the electric conductor to be in direct contact to the biomolecular binding event. Even the smallest binding events influence the charge carriers in the graphene and modulate the signal, ready for measurement. Biological detection systems, such as mammal noses or even the bees' ability to detect single odorant molecules are so fascinating and efficient, scientists have been trying to imitate these sensor systems. But a smell is much more than just detecting a single molecule; it is more like creating a picture composed of the stimuli of the nervous system present as receptors in the nose. The human nose has about 400 receptors able to distinguish more than one trillion different odors [2]. This extremely high number is the result of receptor combinations with different signal magnitudes and stimulation varieties. The nose, like the eyes, contains special receptors, which are all needed to send signals for a specific odor. However, the way the eyes work is easily understood, as they have only four different receptors for colour and brightness. The imitation of the eyes receptors is well known as CCD or CMOS chips, where each pixel represents a point of a projected image on a chip, able to discriminate between brightness and wavelength of the light. A *pixel* for detecting odors has not been developed so far, and leads to the following question: how can one create an electric signal corresponding to the intensity of a specific odor? Once this question is question is answered, a camera-like system could be established with more than just one of those pixels, leading to combinations of odorants and creating a digital image of the present odor. One approach of such an odorant detection system is documented in this work, showing how graphene and an odorant binding protein from the Apis mellifera (western honey bee) are combined in a field-effect transistor to detect specific odorant biomolecules. The electrical measurement of biological binding events was performed utilizing impedance spectroscopy for the measurement of the response of the system at frequencies from 1 Hz to 500 kHz. An illustration of the gFET for odorant detection is shown in Fig. 1.1, measuring the odorant's concentration in a aqueous solution.

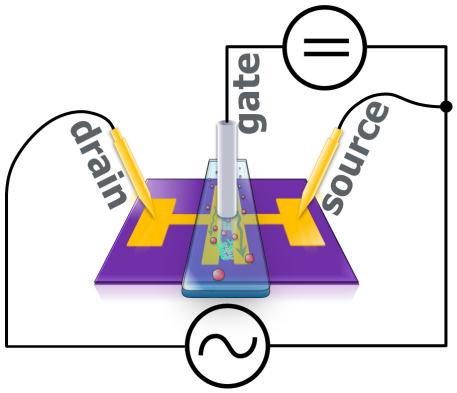

Figure 1.1: Graphene based field-effect transistor with immobilized odorant binding proteins, including electrical set-up to measure the response for odorant presence.

2 Theory

2.1 Graphene

Finding new technologies sometimes requires already known and simple methods. Sometimes a breakthrough in science may result from an unexpected happening as it did in physics: applying scotch tape to a block of graphite and pulling it off, results in thin layers of graphite being adhered to the tape. By repeating this procedure the material is broken down to its minimum: a one atom thick layer of carbon atoms. These atoms are arranged in a hexagonal lattice and form a two-dimensional crystal, called graphene. In 2004, Andre Geim, Kostya Novoselov and co-workers produced graphene with the scotch tape method and started their first investigations [3]. In 2010 they were awarded the Physics Nobel prize because they demonstrated the existence of a two-dimensional crystal - graphene - against the theory of many other physicists. The reason for the stability of two-dimensional crystals was later on shown by thorough investigations on the rippling of graphene sheets. Studies by transmission electron microscopy revealed, that the sheets are not perfectly flat. The roughing arises up to 1nm out-of-plane of the crystal structure and provides an explanation for its stability [4][5]. Graphene sheets consist of sp^2 hybridized carbon atoms. Each carbon atom shares three electrons with its neighbouring carbon atoms and forms strong σ-bonds. A fourth electron in the p-orbital, perpendicular to the graphene surface, has the ability to form weaker π-bonds. Since this electron is not permanently linked to any other atom, it gives graphene the ability to become a semi-metal and to conduct electricity very well. This stands in contrast to any diamond structure, where all atoms are sp^3 hybridized and σ-bonded with all four electrons to the lattice of the diamond, leading to a non-conductive material with a large band gap [6]. Each graphene sheet can form a stack with other graphene layers through $\pi - \pi$-stacking, leading to a multi-layer of graphene. The carbon material is called graphene up to a stack of 10 layers. Fig. 2.1 shows the four types of possible carbon structures

with the two-dimensional graphene on the right side.

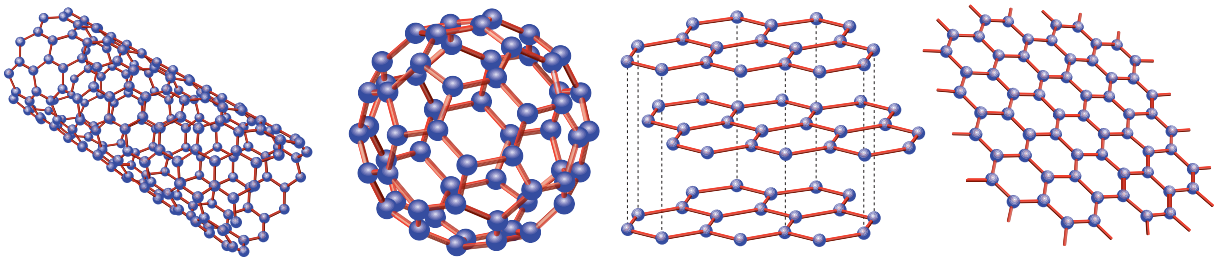

Figure 2.1: [3] Illustration of various carbon allotropes. From left to right: carbon nanotubes, fullerene, graphite and graphene. Nanotubes are rolled-up cylindric graphene sheets. Fullerene (C_{60}) has a ball-like structure, introducing some pentagons and graphite is the $\pi - \pi$-stacking of graphene monolayers.

Beside the fact that graphene is a two-dimensional atomic crystal, it shows extraordinary properties, such as high mechanical elasticity and being the strongest material in respect to its area ever measured [7]. Optical properties allow the manipulation of light transmission through external electric or magnetic fields on the graphene layer, shown by [8]. There are even more unique properties, such as the possibility of forming a gas barrier and the ability to use it as a gas sensors to detect ammonia [9] and last but not least the electric, more precisely the semi-conducting properties of graphene sheets.

2.1.1 Electrical properties

The outstanding electric property of graphene is the reason why this material has gained so much attraction in the last years. It is promising to replace other conducting and semi-conducting materials by graphene or to develop new applications. Up to a bilayer of graphene sheets, the electronic spectra can be seen as a zero-gap semiconductor, or a zero-overlap semi-metal, with one side forming an electron hole and the other an electron donator. This simplified electronic property can not be noticed if more graphene layers are stacked, because then several charge carriers appear and the model becomes much more complex [10]. Furthermore the electrical pathway through single and double layer graphene is not isotropic, meaning the electrons cannot propagate in every direction with the same conductivity. Parallel to the surface the conductivity is about a hundred times greater than across the crystal plane [11].

In Fig. 2.2 (a), the hexagonal structure of graphene is shown, carbon atoms are depicted with blue and yellow circles. It can also be seen as a triangle lattice, with the basis of two atoms. The lattice vectors are called a_1 and a_2, they form the hypotenuse of the triangle and have a length of approximately 1,42Å. Right beside the atomic structure in the same figure, the Brillouine-zone is shown, which corresponds to the reciprocal lattice of the hexagonal structure. In this model the most important points are the K and K' points, the only connection points for the electronic π- and π*-bands at the Fermi level. Wallace et al. calculated the energy needed for an electron to hop from one atom to its nearest neighbour and the next nearest neighbour on this lattice model, already in the year 1947. He calculated the band structure for a single layer and derived an equation, that allows the symmetry of the π- and π*-bands if the kinetic energy to the next nearest neighbour is zero. Fig. 2.2 (b) demonstrates the energy spectrum of

the π- and π*-bands of the complete Brillouine zone, where the unique properties of graphene stem from. At the junction of the two bands, the kinetic energy for electron transition is zero, so the electron are free to move. In this particular figure the symmetry is not given, since it was calculated with a finite value for the transition energy to the next nearest neighbour [11] [12].

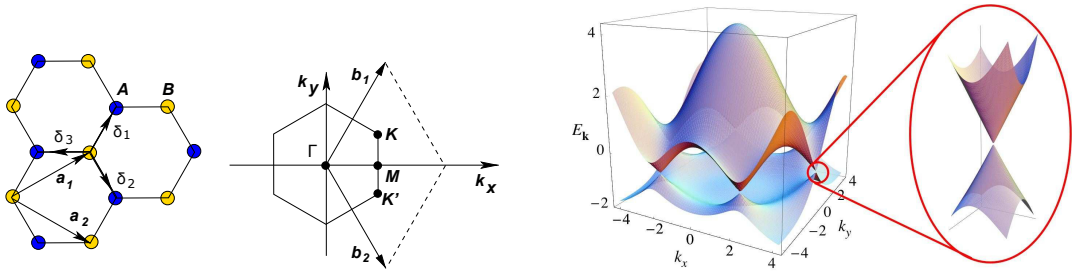

(a) Graphene structure model and corresponding Brillouin zone

(b) Unique band structure of graphene

Figure 2.2: [12] Atomic structure (a) and electronic bands (b) of graphene, indicating that the π- and π-bands meet at K and K' points. The zoom window shows the presence of the dirac point with the zero-bandgap.*

Fig. 2.3 (a) shows the behaviour of graphene in the presence of an electric field, occuring in a field-effect transistor with graphene drain-source channel. The conductivity σ in $k\Omega^{-1}$ of the graphene monolayer changes as the gate voltage V_G changes, while V_G is proportional to the electric field [13]. The conductivity increases in the negative and positive regime of V_G. This shows an ambipolar semi-conducting behaviour of electron and hole mobilities.

Novoselov et al. described the massless fermions in graphene with quantum electrodynamics, as a combination of quantum mechanics and relativity theory, proposing a gas of free massless Dirac fermions for the electrons in the conductive layer [13]. Therefore, the electrons are free to move and give graphene its semi-conductive properties. The hall coefficient $1/R_H$ shows a transition between electron and hole carriers in graphene at the Dirac point around zero volt of V_G, shown in Fig. 2.3 (b), representing the unusual quantum transport phenomena of graphene.

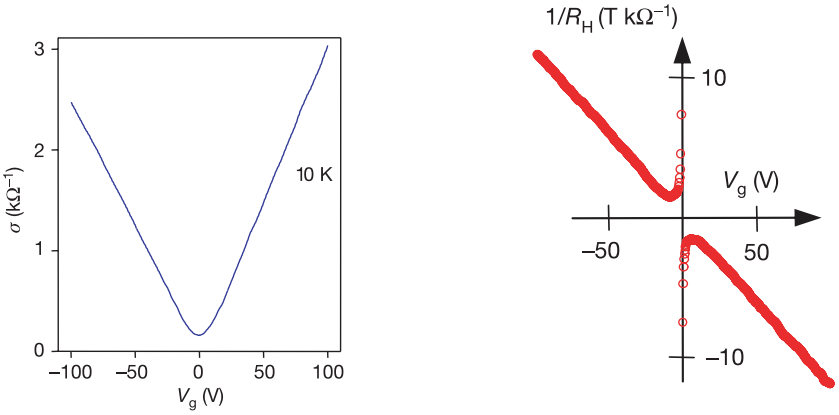

(a) Conductivity σ vs. V_G

(b) Hall coefficient $1/R_H$ vs. V_G

Figure 2.3: [13] Electric field applied to graphene in a field-effect transistor. The left image shows the conductivity, depending on the gate voltage, representing the electric field applied to graphene. On the right side is the hall coefficient of graphene $1/R_H$ vs. gate voltage V_G.

2.1.2 Fabrication of graphene

Adhesive tape peeling method

A simple approach to get a thin or monolayer of graphene is adhesive tape or scotch tape method. This is a micromechanical cleavage method, that peels off some layers of graphene step by step, leaving only a monolayer of graphene at the end. This is the same technique that allowed the fabrication of graphene for the first time by Novoselov et al. [14]. These graphene flakes, up to a size of 100 μM [15] can be transferred to a silicon wafer and the scotch tape is washed off by acetone afterwards.

Chemical vapor deposition

Another approach to get monolayers of graphene is a bottom up technique, called chemical vapor deposition. This technique allows the growth of thin graphene flakes directly on copper foil by a surface-catalyzed process. The foil is heated up to a temperature of 1000°C under vacuum and then methane or ethene gas is introduced for a certain period to grow only a monolayer of graphene on the copper foil. This technique results in high-quality graphene with a size of 1 cmx1 cm [15].

Wet chemical method

The wet chemical protocol to obtain monolayers from graphite flakes was first described by Brodie et al. in 1859 [16] and later refined by Hummers et al. [17] for a safe process in laboratory. This method actually produces graphene oxide flakes, that can be reduced back to graphene. This method uses conventional graphite flakes, an oxidation step to loose the sp^3 bonds of the graphene sheets and then mechanically shear off the flakes by mechanical forces, e.g. ultrasonication or steering. The wet chemical method is highly suitable for low cost and large scale production of graphene with a high variety in flake size up to 100 μm. The exfoliated graphene oxide (GO) monolayers are dissolved in water, applied on silicon wafers in a laboratory environment and then reduced to graphene to get a conducting material, as shown by the group of Larisika et al. with the modified Hummers' method [18].

2.1.3 Reduction of graphene oxide

A reduction process is required to reduce the graphene oxide (GO) of the modified Hummers' method to graphene. The obtained graphene is then called reduced graphene oxide or rGO, and is a conducting material. Commonly used reduction methods are thermal and chemical reduction, where thermal annealing is carried out by thermal irradiation on graphene, called thermal reduction [19]. This can be either performed under exposure of argon gas at 1050 °C [20] or hydrogen gas at 800 °C [21]. Even microwave reduction [22] and photo reduction [23] can be performed to achieve the thermal annealing effect on reduced graphene. The heating of graphene makes the oxygen containing groups on the graphene oxide flakes decompose into gas, but has the disadvantage of producing wrinkled and small flakes compared to other reduction methods.

Chemical reduction can be performed with the use of hydrazine [24] or dimethylhydrazine [25]. These are both strong reduction agents, with the disadvantage of being highly hazardous and therefore less practicable in laboratory use. L-ascorbic acid (Vitamin C) [26] and hydriotic acid [27] are non-hazard reduction methods and are very effective. Especially the hydriotic acid leads to great conductivity and little defects in the graphene flake surface, apart from possible iodine residue. It can be said, that for each application, the appropriate reduction method has to be performed. For the purpose of high electric conductivity, the reduction with hydrazine or hydriotic acid (HI) should be performed.

2.2 Field-effect transistor

Field-effect transistors are used in a wide range of applications, due to their versatility. A field-effect transistor is an active device, able to control the conductance between two terminals (drain and source) applying an electric field. The electric field is evoked by applying a voltage to a third terminal, called gate. If the drain-source channel conducts at zero gate voltage $V_G = 0$, the FET is a depletion type, whereas an enhancement type increases the channel conductivity with raising V_G. The field-effect transistor is called n-type, if electrons are entirely responsible for the conductivity of the drain-source channel, where an p-type FET conducts due to the hole mobilities [28]. A field-effect transistor with hole and electron mobility is furthermore called ambipolar [29]. Dependent on the used substrate and the semi-conducting material, different types of FETs were produced, e.g. JFET, MOSFET, DEPFET, TFET. These differ in mobility-types, the doping of the semi-conducting material or can be distinguished by their insulation material between channel and gate. The main advantage of FETs is low channel current for deactivated devices and the increase of signal to noise ratio compared to bipolar junction transistor [30].

The principle design of a FET consists of three terminals, drain, source and gate. The drain and source terminals are the connection to the conducting channel and the gate electrode, insulated from the channel, controls the conductivity via an electric field. The gate voltage is applied between gate and one of the two source-drain terminals and an ideal FET has no gate current I_G, due to perfect insulation. Fig. 2.4 illustrates the concept of a metal oxide field-effect transistor (MOSFET). There the insulation material is a non-conducting metal oxide, with a thickness of less than 40nm [31].

The MOSFET in Fig. 2.4 (a) has two n-type terminals for drain and source and a p-type substrate, forming the inversion layer, also called the channel region. A metal oxide applied on top of the substrate to insulate the gate electrode from the semi-conducting region gives the MOSFET its name. An applied gate voltage V_G greater than the threshold voltage V_{TN} creates an electron inversion layer and the current flow from source to drain is possible, see Fig. 2.4 (b). The threshold voltage V_{TN} is the minimum *turn on* voltage applied to gate and source, so the concentration of the inversion charge is high enough to create a conducting channel between drain and source.

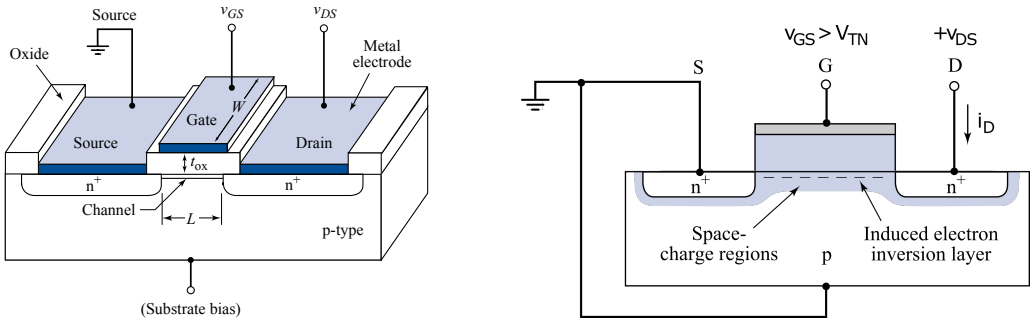

(a) n-channel MOSFET (b) MOSFET with applied V_G

Figure 2.4: Schematic diagram of a metal oxide field-effect transistor MOSFET (a) and (b) shows the electron inversion layer, evoked by applying a gate voltage V_G greater than the treshold voltage V_{TN} [31].

2.2.1 Other FET types

Beside the MOSFETs, also organic FETs (OFETs) with an organic material [32][33] as drain-source channel and nano FETs with other materials such as graphene [34][35], carbon nanotubes [36][37], nanowire [38] or polymers [39] have been developed. These types of field-effect transistors have drawn much interest for the application in biosensing over the past few years, because they allow label-free detection of biomolecules, such as DNA, toxins, viruses, bacteria, hormones and antibodies in nano-scale and they are an effective alternative to optical state-of-the-art detection methods.

A variety of targets can be immobilized on the biosensing FET to modulate the electric field applied to the drain-source channel. Hence, the number of drain-source channel charge carriers will increase or decrease with the presence of selective molecules and this can be directly assessed with the change of current I_D due to conductivity change of the FET [40]. Such field-effect transistors for detection of bio-molecules or bio-recognition events are called Bio-FETs [40].

Fig. 2.5 (a) illustrates the change of conductivity between drain and source depending on the electric field of the environment. The presence of charged molecules influences the conducting surface of the Bio-FET and modulates the current I_D.

Ion-selective FETs are the most basic Bio-FETs and were developed to detect specific ions [41][42], where the protonation and deprotonation of compound material and its hydroxyl groups can be measured. As a second generation of Bio-FETs enzyme reaction-coupled FETs (En-FET) and immuno-reaction coupled FETs (Immuno-FETs) were developed. En-FETs operate using the charged species of the reaction product of enzymic reactions [43][44], while Immuno-FETs react on the change in charge distribution on the gate surface [45]. This redistributions are caused by antigen-antibody reactions and protein-ligand binding actions leading to charge displacement due to conformational changes.

The geometrical set-up of Bio-FETs is different to conventional field-effect transistors. MOSFETs have an insulation layer between the channel and the gate electrode on top, called top gate. Bio-FETs usually have a set-up with a liquid gate or a back gate, shown in Fig. 2.5 (b).

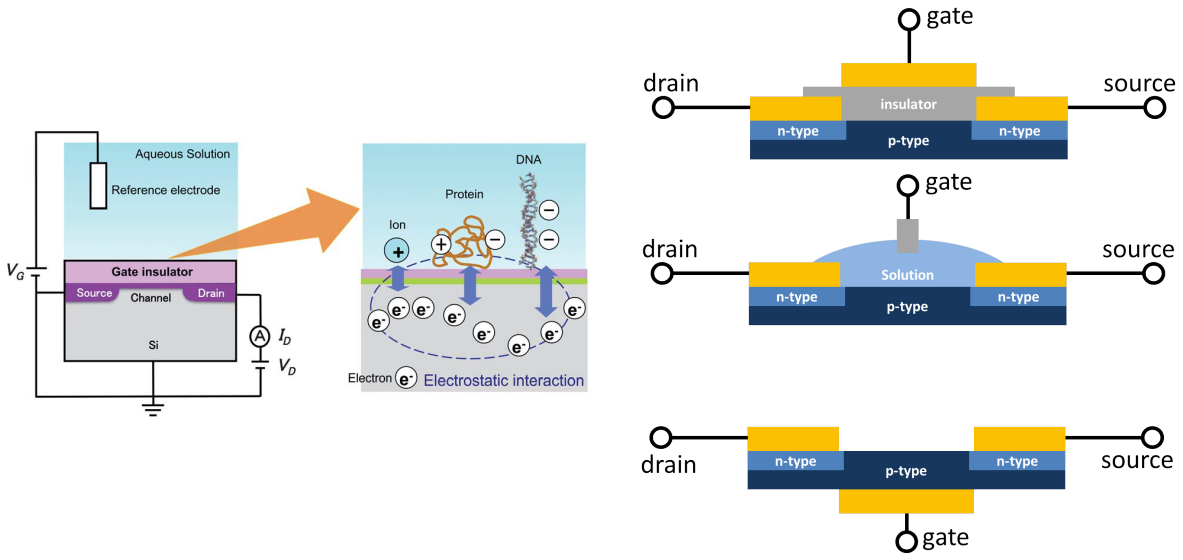

(a) Structure and principle (b) FET types

Figure 2.5: The structure and the working principle of a Bio-FET (a) [40], where bio-molecules are attached on the semiconducting surface. The electrostatic interaction influences the electron transport in the drain-source channel. Different geometrical types of field-effect transistors are shown in (b). A top gate, a liquid gate and a back gate FET are illustrated.

Liquid gate

A liquid gate FET is used to wash an analyte over the channel surface, influencing the electric field to modulate the drain-source current I_D. Usually an electrolytic buffer solution is employed to solve the biomolecule analyte and reduce pH-value changes, and functions as the insulating layer for the gate electrode at the same time.

Back gate

The back gate FET configuration is used to apply the sensitive area directly to the analyte site without having a gate electrode blocking. The gate electrode is insulated from the channel by av silicon oxide layer, which has to be in a scale of several nanometers, otherwise the gate voltage has to compensate for the greater distance to the drain and source terminals.

2.2.2 Graphene field-effect transistor

Field effect transistors, using graphene as a channel material are called gFETs. As mentioned before, graphene has unique electrical properties, opening a new regime between conductor and semi-conductor. If an electric field is applied across a graphene layer, it shows electron and hole mobilities, therefore it is an ambipolar material. The ambipolarity was theoretically and experimentally shown for graphene field-effect transistors by several groups [46][47]. Hence, the control of the drain current I_D by adjusting V_G differs in the applied voltage regimes. In one range the gFET shows n-type behaviour, with increasing channel conductivity, respectively I_D with increasing V_G, whereas the p-type gFET reduces I_D with increasing V_G. The electrical

characterization of graphene FETs is done by $I_D V_D$ and the $I_D V_G$ curves, where the drain-source current I_D dependency to drain-source voltage V_D and gate voltage V_G is shown [18].

gFET as a Barristor

High on/off ratio can be achieved through the zero bandgap of perfect graphene, needed for logic functions in circuits. A device with a high electron barrier between two terminals that can be modulated by a third terminal, applying an electric field to decrease the barrier, is called a barristor. A graphene barristor can be used as switch for logic electronics, due to its significant different conductivities between *on* and *off* by a factor of 10^7 [48].

2.3 Biosensor

The definition for biosensors after IUPAC is

> "A device that uses specific biochemical reactions mediated by isolated enzymes, immunosystems, tissues, organelles or whole cells to detect chemical compounds usually by electrical, thermal or optical signals." [49]

2.3.1 Graphene FET as biosensor

Therefore, a biologically functionalized gFET, able to detect molecules at specific biochemical reactions, is a biosensor. A biosensor consists of a biotransducer that converts a chemical signal to an electrical or optical signal, ready to measure. The biotransducer is the interface to the biological system and contains a bio-recognition layer to detect enzyme reactions, protein bindings or antigen-antibodies reactions. The gFET's biotransducer element is graphene, while the immobilized biomolecules, e.g. antibodies, proteins or aptamers, which specifically react with targeted molecules are the receptors. The transformation of this biological binding event to an electrical signal is based on two different working principles:

1. Modulation of the electric field through the presence of analytes, proteins, biomolecules etc.

2. Surface charge of graphene changes through conformation changes of proteins or charge displacement.

The effect of electric field modulation caused by the analytes in solution is negligible compared to the surface charge changes. While the saline solution *screens* the electric field, it remains constant and does not modulate the signal over time. The term *screening* describes the damping of electric fields due to charged carriers in solution, i.e. the ions. This effect is called Debye screeing, described in Section 2.3.3. The immobilized biomolecules attached on the graphene surface (the receptors) perform a charge redistribution leading to a change in conductivity of the transducer element between drain and source. The electric field enhances this effect significantly

and leads to a quantitative or semi-quantitative information of the presence of an analyte. The chemical or biological information is converted into an electrical signal, ready to be measured [50].

2.3.2 Protective layers on gFET

To reduce the undesired gate-source current in field-effect transistors, high-k materials are used to insulate the gate terminal and decrease the drain-source leakage through tunneling. The term *high-k* stems from the Greek letter for the dielectric constant κ, also called ϵ_r. For miniaturization of FETs, the insulating capacity C_i has to stay constant, otherwise the leakage current increases. C_i is calculated by equation(2.1):

$$C_i = \epsilon_0 \cdot \frac{\kappa}{d} \tag{2.1}$$

where ϵ_0 is the permittivity in Fm^{-1} in free space, κ the unit free relative permittivity and d the thickness of the insulator material in m [51]. Due to the reduction of d, κ has to be increased to keep a constant gate capacity C_i.

The dielectric material of conventional FETs is SiO_2 with $\kappa_{SiO_2} = 3.9$ [52]. So-called passivation layers are applied to achieve a pinhole free insulating surface with a high relative permittivity ϵ_r. Such high-k materials are for example Al_2O_3 $\kappa = 9.5$ [53], TiO_2 $\kappa = 40$ [54] or Ta_2O_5 $\kappa = 100$ [55]. These metal oxide layers are applied between the drain-source channel and the gate electrode by atomic layer deposition (ALD) [56], anodization, sputtering, e-beam or evaporation. These insulating layers reduce the influence of the undesired gate current I_G to the analyte in liquid gated FETs. Beside these aspects, a protective layer should increase the distance from analytes to the graphene surface, so the conductivity of graphene cannot be directly influenced by the adhesion of ligands. That should reduce the unspecific response of gFETs.

Other layers to prevent the detection surface to be directly in touch with the analyte are organic layers, such as crystalline bacterial cell surface layer (S-layer) or blocking agents like PEG (polyethylen glycol) and BSA (bovine serum albumin). PEG and BSA blocking agents are used to saturate all left binding sites on ELISA applications to prevent unspecific binding actions [57][58].

2.3.3 Debye length

Due to the planar surface of graphene, with attached biomolecules in contact with a saline solution, an electric double layer forms out. The double layer is formed by two parallel layers of charges on top of graphene. Within this double layer, the biomolecules interact with the analyte in solution, with the detectability of these events depending on the Debye screening length. The Debye screening length λ_D, short Debye length describes the electrostatic distance, decreasing the electric potential by $1/e$ every λ_D. The reason for a damped electrostatic interaction of a charge Q is the shielding or screening of surrounding charged particles. The square root of the concentration of charges in an electrolyte solution is inversely proportional to the Debye length.

The Debye length for water at 25 °C and a monovalent salt concentration can be calculated with equation (2.2) [59]:

$$\lambda_D = \frac{3.04 \text{ Å}}{\sqrt{c_0 \frac{L}{mol}}} \tag{2.2}$$

where c_0 is the concentration in mol/L and λ_D the Debye length in m. Therefore, the presence of ions in solution decrease the ability of two molecules to interact. In a 0.1 M NaCl solution, the Debye length is only 0.96 nm. The Debye length for solutions with several different ions with higher valencies can be calculated with equation (2.3),

$$\kappa = \sqrt{\frac{e^2}{\epsilon\epsilon_0 k_B T} \sum_i c_i^0 Z_i^2} \tag{2.3}$$

where κ is the inverse Debye length in 1/m, e Euler's number, ϵ the dielectric constant, ϵ_0 the vacuum permittivity, k_B the Bolzmann constant and T the temperature in K. Z_i is the valency of the i^{th} ion sort. In other words, the Debye length represents the distance within which a molecules is able to interact with another desired molecule. The ion concentration of electrolytic solutions is determining the electrostatic interaction radius of biorecognition molecules with analytes, therefore it has to be taken in consideration for the choice of the solution, containing the analyte.

2.3.4 Langmuir adsorption model

To describe the kinetics of binding reactions, such as antigen to antibody or protein to ligand, the Langmuir adsorption model has been widely used for biosensor applications [60][61]. This model describes the adsorption of ligands on a solid surface with a finite number of binding sites at a certain pressure, volume and temperature. [62].

To be able to apply the Langmuir adsorption model, the parameters K_A and K_D have to be introduced. The usage of the Langmuir adsorption model requires three assumptions:

1. Only monolayer coverage is possible,
2. homogenous surface,
3. neighbouring binding sites do not influence the adsorption of one binding site and
4. equivalence of all binding sites.

If all conditions are met, the binding equilibrium can be written as

$$A + B \underset{k_{off}}{\overset{k_{on}}{\rightleftharpoons}} AB \tag{2.4}$$

where A is the analyte and B is the immobilized receptor [63]. The forward reaction, the adsorption, is described by the association rate constant k_{on} in $M^{-1}s^{-1}$, while the reverse reaction, the desorption, is associated with the dissociation rate constant k_{off} in s^{-1}.

At a dynamic equilibrium, the rates of association and dissociation are equal, (2.5):

$$k_{on}[A][B] = k_{off}[AB] \tag{2.5}$$

Under these assumptions, the measured data of different analyte concentrations can be used to calculate the association and dissociation rate constants for comparison of measurement to data from literature. Furthermore, the affinity and dissociation constants K_A and K_D can be evaluated with equations (2.6) and (2.7) [63],

$$K_A = \frac{[AB]}{[A][B]} = \frac{k_{on}}{k_{off}} \tag{2.6}$$

$$K_D = \frac{[A][B]}{[AB]} = \frac{k_{off}}{k_{on}} \tag{2.7}$$

where K_A in M^{-1} is the inverse of K_D in M.

The Langmuir adsorption model describes the surface coverage, where θ is the percentage of formed complexes AB with respect to the total amount of binding sites B. Therefore, 1 - θ is the number of free binding sites and equal to [B]. Equation (2.8) describes the fraction of the concentration of the complex AB to the concentration of B.

$$\frac{[AB]}{[B]} = \frac{\theta}{1-\theta} \tag{2.8}$$

Regarding equation (2.6), equation (2.8) is equal to

$$K_A \cdot [A] = \frac{\theta}{1-\theta} \tag{2.9}$$

Under the assumption of an infinite reservoir of [A], due to a constant inflow of the analyte A, [A] can be expressed as a constant c. Substitution into (2.9) and rearrangement yields θ according to equation (2.10). This equation is called Langmuir isotherm and is only valid for a system with constant temperature, pressure and [A].

$$\theta = \frac{c \cdot K_A}{1 + c \cdot K_A} \tag{2.10}$$

In Fig. 2.6 the linear and exponential Langmuir isotherm representation of measured data is shown. At 50% surface coverage the dissociation constant K_D is obtained. The Langmuir

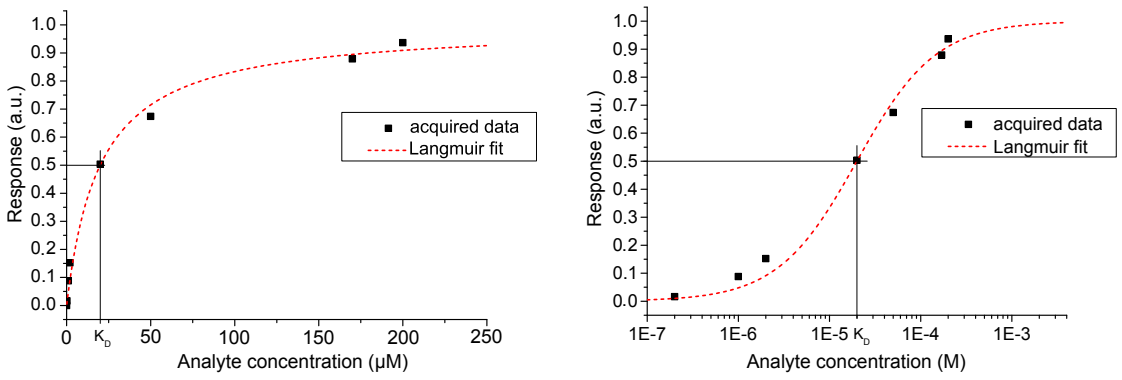

(a) Linear Langmuir fit

(b) Logarithmic Langmuir fit

Figure 2.6: The Langmuir fit applied to acquired data points to determine the dissociation constant K_D. K_D can be observed at 50% of surface coverage. At this value, 50% of all binding sites B formed a complex with the ligand A.

isotherm fit can be used for biosensor calibration by reference measurements with a known analyte concentration. Furthermore, the saturation of the surface can be evaluated, as well as the surface density of receptors. Beside the quantification of analytes or receptors binding to a surface, the Langmuir isotherm fit is an important tool for comparison of different biosensors. It can be also used to optimize specific sensor types. Due to the evaluation of surface coverage θ with the Langmuir isotherm equation, the results of different measurement systems can be compared. The surface coverage at a certain concentration should be the same for electrical, optical or any other measurement method.

Linear equation for k_{obs}

The biomolecular interaction of an analyte A with an immobilized receptor B, forms a complex AB under the association and dissociation rate constants k_{on} and k_{off}. A new parameter for the binding kinetics is introduced, called k_{obs}. This parameter is given by the linear equation (2.11), determined by k_{on}, k_{off} and the ligand concentration [A] [63],

$$k_{obs} = k_{on} \cdot [A] + k_{off} \tag{2.11}$$

where k_{on} represents the slope and k_{off} the intercept.

A change of [AB] over time is the result of association of [A] with [B] to [AB] and dissociation of [AB]. The derivative of [AB] with respect to the time is given by equation (2.12)

$$\frac{d[AB]}{dt} = k_{on}[A][B] - k_{off}[AB] \tag{2.12}$$

where the association with the rate constant k_{on} leads to an increase of [AB] and the dissociation with the rate constant k_{off} decreases the concentration of the AB complexes [63].

Due to an infinite reservoir of analyte A, the concentration [A] remains the same as initially: [A] = [A_0]. The concentration of the formed complex AB decreases if more binding sites B are free, while B_0 is the total number of binding sites: [AB] = [B_0] - [B]. Substituting these

relationships in equation (2.12) and integrate it over time equation (2.13) is obtained.

$$\int_{t_0}^{t} \frac{d[AB]}{dt} dt = \int_{t_0}^{t} ([B] \cdot (k_{on}[A] + k_{off}[B]) - k_{off}[B_0]) dt \tag{2.13}$$

After introducing k_{obs}, equation (2.14) can be obtained.

$$\int_{t_0}^{t} \frac{d[AB]}{dt} dt = \int_{t_0}^{t} ([B] \cdot k_{obs} - k_{off}[B_0]) dt \tag{2.14}$$

Under the assumption of $k_{off} \ll k_{obs}$, it can be simplified to

$$\int_{t_0}^{t} \frac{d[AB]}{dt} dt = \int_{t_0}^{t} [B] \cdot k_{obs} dt \tag{2.15}$$

On the other hand, the derivative of [AB] can be expressed as the derivation of $[B_0]$ - [B]

$$\frac{d[AB]}{dt} = \frac{d[B_0]}{dt} - \frac{d[B]}{dt} \tag{2.16}$$

while the concentration of B_0 remains constant over time. Substituting this result in equation (2.15), equation (2.17) can be obtained

$$\int_{t_0}^{t} -\frac{d[B]}{dt} dt = \int_{t_0}^{t} [B] \cdot k_{obs} dt \tag{2.17}$$

resulting in equation (2.18) for the exponential fit of binding kinetics for a specific concentration.

$$[B] = [B_0] \cdot e^{-k_{obs} \cdot t} \tag{2.18}$$

According to equation (2.18) k_{obs} can be obtained through an exponential fit to the data and afterwards the concentration [A] can be extracted due to its linear dependence with kobs, shown in Fig. 2.7 (a). The observed parameter k_{obs} for a certain concentration is resulting from this exponential fit and can be plotted against the concentration of the analyte, see Fig. 2.7 (b).

The association and dissociation rate constants k_{on} and k_{off} can be calculated from k_{obs} with equation (2.11). K_A and K_D are calculated with equations (2.6) and (2.7). The values for the calculated affinity and dissociation constants should be in the same order as the one evaluated with the Langmuir isotherm equation (2.10).

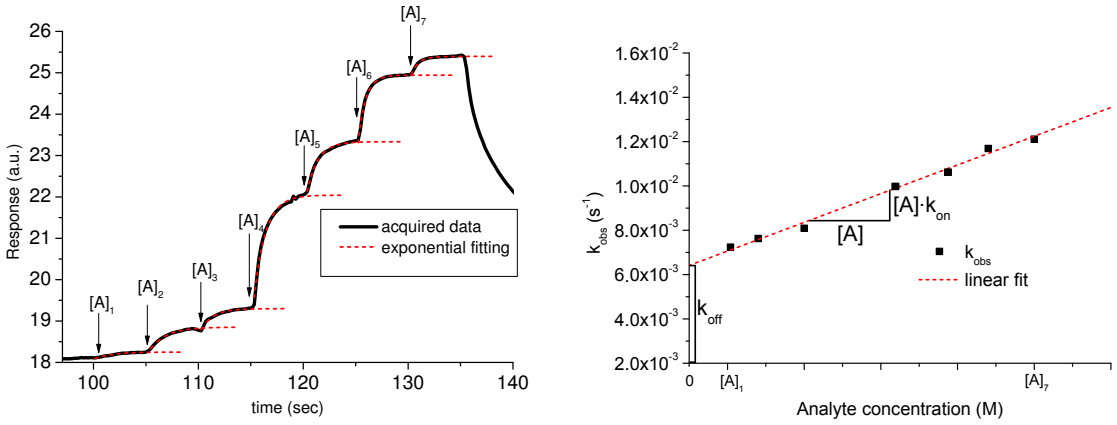

(a) Exponential fit to acquired data

(b) Linear fit of k_{obs}

Figure 2.7: The exponential fit to the acquired data results in the parameter k_{obs} in the exponent. In (a) the exponential fit to every new concentration was performed. Plot (b) shows the corresponding k_{obs} to every concentration. It obeys to equation (2.11) which relates [A] linearly to k_{obs}.

2.4 Odorant binding proteins

Odorant binding proteins (OBP) are able to evoke signals in the odorant receptors, stimulating the olfactory neurons in the nervous system of mammals and insects [64]. These proteins are located in the aqueous phase, the mucus of the olfactory system. With a typical molecular weight of about 20 kDa, these proteins associate with ligands, called odorants. Odorants are small molecules with a molecular weight of 100 to 400 Da, binding specifically to the OBPs. The reversible association and dissociation of odorants with OBPs are demonstrated to have kinetic constants (K_D) in a micromolar range [65]. Recent studies showed the ability of the human nose to discriminate more than one trillion of olfactory stimuli [2]. It demonstrates the high sensitivity and selectivity of OBPs. Numerous studies were done to investigate OBPs in mammals [66] and insects [67]. Some of the investigations are based on the olfactory receptor I7 of rats [68], the antenna OBPs of the silkmoth Bombyx mori [69] and the western honey bee (Apis mellifera) [70], including the affinities to odorants.

The hive workers glands of the western honey bee express OBP14 [71], that has its highest binding affinity to eugenol (K_D = 280 nM). This odorant is the main component of odor of cloves leading to conformational changes of the OBP14. The chemical structure of eugenol is shown in Fig. 2.8 (b).

Structure of OBP14

The group of Paolo Pelosi studied the structure of OBPs, odorants and the biochemical mechanisms of olfactory transducers [64][72]. The conformational change of OBP14, induced by the binding of the odorant eugenol, is demonstrated in Fig. 2.8 (a) [73]. Here the OBP14 is shown in two conformational states: without the presence of any specific ligands (gray) and with the presence of eugenol in the binding pocket (blue).

Transformations of α helices and β sheets due to the binding of specific ligands lead to redistribution of charges on the OPB14, shown in Fig. 2.9. Conformational changes can be

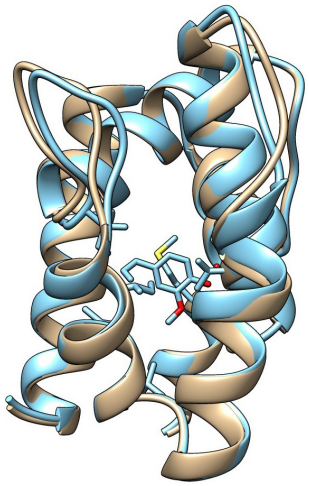

(a) Conformation of OBP14 with and without ligand

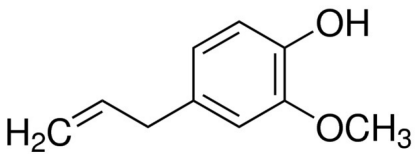

(b) Chemical structure of eugenol

Figure 2.8: Odorant binding protein OBP14 with (blue) and without eugenol in the binding pocket (gray)(a). The conformational change appears due to the presence of eugenol. Unpublished data provided by Christoph Steininger, AIT Vienna, created in UCSF Chimera [74], based on X-Ray data from Spinelli et al. [73]. The chemical structure of the ligand eugenol is shown in (b).

measured either optically with surface plasmon resonance (SPR) [75] [76], fourier-transformed infrared spectroscopy, fluorescence spectroscopy [77], labeled fluorescence displacement, X-ray analysis [73] or mechanically with quartz crystal resonance (QCR) load sensors [78]. Also electrical investigations were performed with BioFETs, employing surface-immobilized OBP14 on graphene to measure the charge displacement with direct current [79].

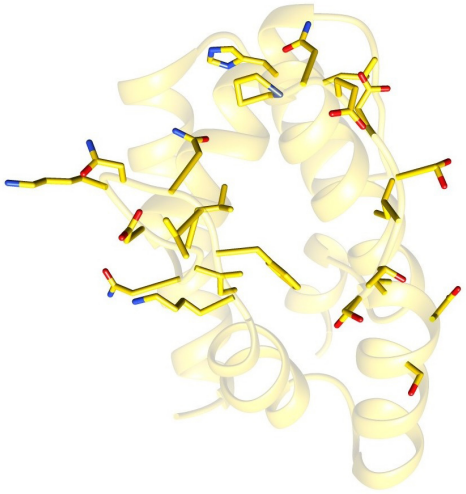

(a) OBP14 charges without eugenol

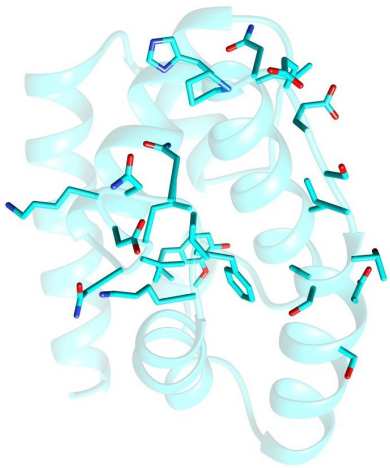

(b) OBP14 charges with eugenol

Figure 2.9: Charge displacement of polar groups due to conformational change of the odorant binding proteins in the presence of eugenol. Only charges with a considerable displacement are shown. The yellow illustration is without and the blue with eugenol in the binding pocket. Unpublished data provided by Christoph Steininger, AIT Vienna, created in UCSF Chimera [74], based on X-Ray data from Spinelli et al. [73].

2.5 Impedance Spectroscopy

Impedance at alternating current is the electrical equivalent to the resistance in direct current. While Ohm's law defines the resistance R in ohm as the fraction of static voltage V in volt and the current I in ampere, the impedance Z is the complex resistance, taking also the phase shift into consideration. The response of an electric system to a given sinusoidal voltage V(t) is the current I(t), where both are dependent on time. The input signal V(t) is frequency dependent, and so is the current I(t), see equation (2.19).

$$V(t) = V_A \; sin(\omega t) \qquad I(t) = I_A \; sin(\omega t + \varphi) \qquad \omega = 2\pi f \tag{2.19}$$

The ratio of input and response is no longer just a magnitude, because also the phase shift φ of the response signal with respect to the input has to be accounted. The complex impedance Z is defined in equation (2.20)

$$Z = \frac{V(t)}{I(t)} = \frac{V_A sin(\omega t)}{I_A sin(\omega t + \varphi)} = Z_A \frac{sin(\omega t)}{sin(\omega t + \varphi)} \tag{2.20}$$

where Z is expressed by the magnitude $Z_A = |Z|$ and the phase shift φ. The phase shift can be either positive or negative, depending on the system's characteristic. The electrical components of the system determine the magnitude |Z| and the phase shift φ for a certain frequency f or a radian frequency ω.

Therefore, a complex impedance Z can be defined and expressed in either magnitude and phase shift, or real an imaginary part Z_{REAL} and Z_{IM} [80].

$$Z = \mid Z \mid e^{j\varphi} = \mid Z \mid (cos\varphi + jsin\varphi) = Z_{REAL} + jZ_{IM} \tag{2.21}$$

Impedance spectroscopy is an electrical measurement technique, acquiring the impedance Z for a set of frequencies in a defined range. While the frequency f in Hz increases in discrete steps, an AC voltage V(t) is applied to the system. The magnitude of the current I(t) and the phase shift between V(t) and I(t) are measured with a lock-in amplifier to calculate the impedance Z for each frequency with equation (2.20). Z can be represented graphically in a Nyquist plot or in Bode plot. The Nyquist plot in Fig. 2.10 shows the components of Z: magnitude |Z|, the phase angle φ, Z_{REAL} and -Z_{IM}.

The Nyquist plot is a useful method to show the magnitude and phase angle in one figure, but the frequency f or ω for each point is usually not marked.

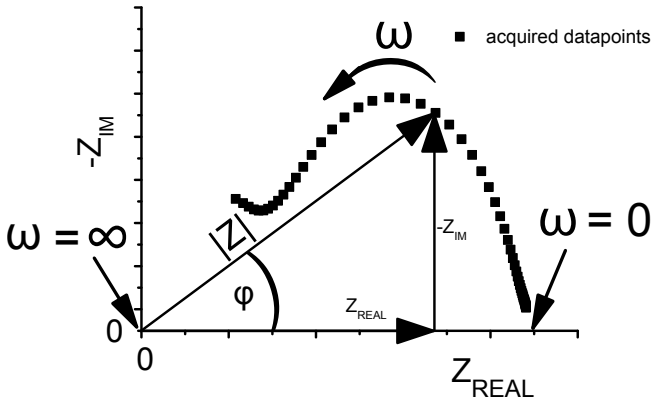

Figure 2.10: Nyquist plot of an impedance spectroscopy measurement, where the components of the complex impedance Z are shown.

2.5.1 Basics components of impedance spectroscopy

As mentioned before, the magnitude and phase angle of Z are given by the electrical equivalent components of the system. These components can be either ideal with a defined phase shift, or non-ideal, changing the phase or magnitude over time due to diffusion, inhomogeneous surfaces or other phenomena [80].

The impedance analysis of a system is an attempt to represent complex mechanisms, e.g. physical, chemical or electrical, with an electrical equivalent circuit, the EEC. As a first approach, it can be represented by ideal components, listed in Tab. 2.1.

Electrical Circuit Elements			
Component	Equivalent Element	Unit	Impedance
Resistor	R	ohm	R
Capacitor	C	F	$\frac{1}{j\omega C}$
Inductor	L	H	$\mathrm{j}\omega\mathrm{L}$
Constant phase element	Q	$\mathrm{ohm}^{-1}\mathrm{s}^{\alpha}$	$\frac{1}{\mathrm{Q}(\mathrm{j}\omega)^{\alpha}}$

Table 2.1: Components of electrically equivalent circuits for modeling real systems.

Ideal circuit elements

An EEC with only ideal components, such as R, C and L leads to a defined response of the equivalent system. The impedance of R is independent of frequency and remains constant over the entire impedance spectrum. A capacitance C leads to a current phase shift of φ = -90° with respect to the voltage, while an ideal inductance shifts the current for +90°.
Unfortunately, real systems suffer from non-stationarities and cannot be modeled with R, C and L. Therefore, the constant phase element is introduced.

Non-ideal circuit elements

For the representation of real-life phenomena in impedance analyses, equivalent elements like the constant phase elements (CPE) are introduced. Equation (2.22) describes the impedance Z_{CPE} [80]:

$$Z_{CPE} = \frac{1}{Q(j\omega)^{\alpha}} \tag{2.22}$$

For $\alpha = 1$, the impedance of the CPE equals to an ideal capacitor, while $\alpha = 0$ represents an ideal resistor, independent of f. For any other value of α the constant phase element is a parallel circuit of frequency-dependent components C(f) and R(f). Another special case is when $\alpha = 0.5$, where it is called the Warburg diffusion, which is often defined for electrode boundary conditions [80]. The CPE allows an adaptation of the EEC to a real system, changing with e.g. analyte concentrations, temperature or pressure. Due to the distribution of currents in an electroactive species, the capacitances in many experiments undergo a non-ideal frequency behaviour and have to be replaced by a CPE. One example for such a capacitance is the double-layer capacitance C_{DL}.

2.5.2 Electrochemical double-layer capacitance C_{DL}

Between the electrode of a measurement chamber and its electrolyte an electrochemical double-layer will be formed [80, page 69]. It is caused by ions and charged or polarizable molecules in the solution, which will be attracted by the electrodes. Several effects interfere at the surface of the electrodes resulting in formation of different layers of charged molecules. Depending on the geometrical distance to the electrodes the double-layer is separated into three compartments: 1. the Helmholtz layer, 2. the diffusion layer and 3. the bulk solution, Fig. 2.11.

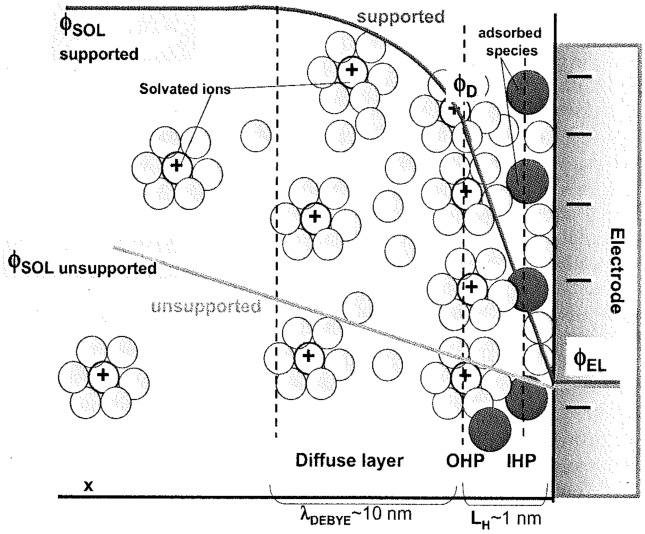

Figure 2.11: [80, page 70] The double-layer capacitance formed between the electrode surface and the bulk solution. Electrostatic forces attract charged molecules to the surface, forming an electric capacitance C_{DL}.

Helmholtz layer

The polar molecules will be adsorbed by electrostatic attraction to the very near area at the electrodes and form a first layer, also called the *Stern* layer.

Diffuse layer

The electrostatically attracted species above the first adsorbed layer are attached with less adhesion and tend to diffuse in solution again, so this layer is called the *diffusion* layer.

2.5.3 Impedance spectroscopy applied to biomolecules

In previous works, impedance spectroscopy was employed to measure cell growth [81], label-free aptamer binding or enyzme activity detection with mechanisms similar to antigen-antibody interactions [82] [83] and for the determination of human immunoglobulin G [84]. The detection of any biological event varies from dielectric dispersion in human cells to the change in charges at a surface of a nanocomposite. The impedance spectroscopy measurement for biological events is a promising tool to get more information and higher specificity due to a larger scope of analysis, compared to DC measurements.

3 Materials and Methods

3.1 Material

All required materials and chemicals for the synthesis of graphene oxide (GO), the reduction to rGO, the fabrication of field-effect transistors, measurement of graphene FETs and for immobilizing biomolecules on the graphene surface are listed in this chapter.

3.1.1 Materials for graphene oxidation

- Graphite flakes size 2 - 5 mm, NGS Naturgraphit GmbH
- Magnetic stirring bar
- Magnetic stirrer MR Hei-End, Heidolph
- Ultrasonic cleaner S180H, Elma Schmidbauer GmbH
- Membrane filter, pore size 0.45 µm, Membrane Solutions

3.1.2 Chemicals for graphene oxidation

- Sulfuric acid 99.99%, Sigma-Aldrich
- Ammonium hydroxide solution 33%, Sigma-Aldrich
- Hydrogen peroxide solution 30%, Sigma-Aldrich
- DI Water 18.2MΩ, Sartorius Stedium Biotech machine

3.1.3 Materials for reduction of graphene oxide

- Laboratory oven Heraeus B12, Thermo Scientific
- High temperature tape 7412P, 3M
- Glass petri dish 150 mm, Sigma-Aldrich

3.1.4 Chemicals for reduction of graphene oxide

- Hydrazine, Sigma-Aldrich
- Hydriodic acid, Sigma-Aldrich

3.1.5 Materials for gFET production

- Glass chip holder individual construction, Lindeberg
- Thermal evaporator AUTO 306 with FL400 box chamber, HHV Ltd.
- Molybdenum evaporation boats, HHV Ltd.
- Silicium chips 20 x 20 mm^2, 300 nm SiO_2, Sigert Consutling eK
- Chip holder for 25 chips 20x20 mm^2, Carl Roth productions
- Gold evapore mask 0.6 mm AlMg individual construction, Lindeberg
- Chromium granules 2 - 4.7 mm 99.99%, MaTecK
- Gold granules 2 - 4 mm 99.99%, MatecK
- Graphene oxide solution 5 wt%, University of Bayreuth
- Univex 450C, Oerlikon Leybold Vacuum

3.1.6 Chemicals for gFET production

- Ammonium hydroxide solution 33%, Sigma-Aldrich
- Hydrogen peroxide solution 30%, Sigma-Aldrich
- Aminopropyltriethoxysilane, Sigma-Aldrich
- Ethyl alcohol 100%, Sigma-Aldrich

3.1.7 Chemicals for functionalization of the gFET

- Tetrahydrofuran, Sigma-Aldrich
- Pyrenebutyric acid N-hydroxysuccinimide ester 95%, Sigma-Aldrich
- (3-Glycidyloxypropyl)trimethoxysilane 98%, Sigma-Aldrich
- Odorant binding protein 9A, Paolo Pelosi
- Odorant binding protein 9B, Paolo Pelosi
- Odorant binding protein 14, Paolo Pelosi
- Bovine serum albumin, Sigma-Aldrich
- Lysozyme 95%, Sigma-Aldrich

3.1.8 Materials for impedance spectroscopy

- Potentiostat 16-channel VMP3, Bio-Logic SAS
- Flowcell, Lindeberg
- Gold spring contact probes with wires, Tekon Prueftechnik GmbH
- Platinum wire 2.0 mm, MaTecK
- Peristaltic pump, ISMATEC
- IPC high precision multichannel dispenser, ISMATEC
- MXX low pressure valves, Rheodyne
- Tubings (diameter 0.64 mm, length 300 mm), ISMATEC

3.1.9 Chemicals for impedance spectroscopy

- Eugenol, Sigma-Aldrich
- Sodium chloride, Sigma-Aldrich
- Potassium chloride, Sigma-Aldrich
- Disodium hydrogen phosphate, Sigma-Aldrich
- Potassium dihydrogen phosphate, Sigma-Aldrich

3.1.10 Materials for investigation on gFET

- Microskope HR800, Horiba
- Field Emission Scanning Electron Microscope SUPRA™ 40, Zeiss
- Confocal laser scanning microscopy TCS SP5 II, Leica

3.1.11 Chemicals for investigation on immobilization

- Cytochrome *c* Oxidase, Sigma-Aldrich
- Iodoacetamidofluorescein, Sigma-Aldrich
- N-Dodecyl-β-D-maltoside, Sigma-Aldrich
- Potassium ferricyanide, Sigma-Aldrich

3.1.12 Software for measurement

- EC-Lab Ver 10.44, Bio-Logic SAS
- OriginLab 8.5, OriginLab Corporation
- Titan MX™ software, Rheodyne

3.2 Methods

The production methods for synthesizing graphene oxide, application of GO on silicon wafers, the reduction of graphene oxide and the gold electrode evaporization on rGO are explained. All measurement set-ups and software adjustments are listed in this section. Furthermore, the functionalization of the gFET with proteins, the application of protective layers on the gFET and the measurement techniques for biosensing are explained.

3.2.1 Wet chemical graphene synthesis

Based on the modified Hummers' graphite oxidation technique, the protocol of Larisika et al. [18] was used to synthesize graphene oxide. The resulting graphene oxide flakes are monolayer or double-layer sheets, able to be reduced subsequently to the conductive reduced graphene oxide (rGO).

Oxidation of graphite flakes

The first step to get monolayer graphene oxide (GO) sheets from graphite is pre-oxidation. This procedure increases the resulting yield of graphene oxide. Therefore, 2 g of graphite flakes are added to 12 mL H_2SO_4, heated to a temperature of 80 °C and stirred for 4.5 hours with a magnetic stirring bar. Afterwards, the solution is ultrasonicated for 1 hour for mechanical cleavage. The pre-oxidized graphite mix is then separated from H_2SO_4 by filtering with a membrane filter and a pore size of 0.45 µm. In a 1 liter beaker, 120 mL of H_2SO_4, the graphite and a magnetic stirring bar are added. Placing this beaker in a ice bath reduces the temperature of the endothermic process of oxidation. 15 g $KMnO_4$ are added gradually during the next 2 hours to the H_2SO_4-graphite mix for oxidation to GO at 220 rpm stirring. After 2 more hours of stirring at 25 °C, the solution is poured into 250 mL of deionized water (dH_2O) and stirred for another 30 min. 750 mL of dH_2O are added afterwards and the stirring is turned off. As soon as the solution is calm, 20 mL of H_2O_2 are added gradually by pipette, leading to a preticipation reaction. All unoxidized components sink to the bottom of the beaker, while the GO floats on top of the solution. The GO sheets are skimmed gently with a spoon and dissolved in 500 mL of dH_2O and stirred for another 72 hours at 200 rpm. The GO can be stored for up to four weeks in this environment at room temperature before it starts clustering to larger compounds.

3.2.2 Preparation of phosphate-buffered saline

The aqueous bulk solution for analyte measurement is a phosphate-buffered saline (PBS) solution, used to keep a constant pH value for all measurements. The PBS solution is prepared in a laboratory bottle, filled with 1 liter dH_2O and dissolving the chemicals listed below:

- 8.0 g Sodium chloride (NaCl)
- 0.2 g Potassium chloride (KCl)
- 1.44 g Disodium hydrogen phosphate (Na_2HP_4)
- 0.24 g Potassium dihydrogen phosphate (KH_2PO_4)

The resulting buffer has a concentration of 170 mM saline. The stock solution is diluted by 1:10 with dH_2O to obtain 17 mM PBS solution, required for all measurements on the gFET.

3.2.3 Fabrication of graphene field-effect transistors

The field-effect transistor are produced with graphene oxide on silicon wafers. The GO is chemically reduced to reduced graphene oxide (rGO) for a conductive drain-source channel. The preparations of silicon wafers, the application of graphene oxide on the silicon surface, the reduction to reduced graphene oxide and the application of electrodes and protective layers are explained in this section.

RCA cleaning

The RCA cleaning method has become standard practice for cleaning silicon wafers [85]. The cleaning process is necessary to get rid of the remaining adhesive particles at the back of the wafer, dust and organic waste and other contaminations on top of the polished SiO_2 surface. 20 mL of 30% NH_3, 20 mL of 30% H_2O_2 and 100 mL of dH_2O are blended in a glass beaker. 25 silicon chips are placed in this solution and heated to 80 °C for 30 min. The chips are washed with dH_2O and dried with compressed air after.

Application of graphene oxide on SiO_2

To attach graphene on top of the SiO_2 layer it is necessary to prepare the SiO_2 first with a process called silanization. Therefore, aminopropyltriethoxysilane (APTES) is applied on the surface. APTES is a self assambly monolayer (SAM) on SiO_2 surfaces and it creates an adhesive layer for graphene oxide. 50 mL solution of 2% ABTES in pure ethyl alcohol are applied to the SiO_2 wafers in a plastic petri dish for exactly one hour. Afterwards, all chips are washed with ethyl alcohol and then heated at 120 °C for 2 hours. All silicon chips are prepared for graphene oxide attachment.

Dropcasting of graphene oxide on SiO_2

On the previously silanized SiO_2 surface, graphene oxide can be applied. The synthesized GO is floating on top of the dH_2O and can be extracted from the surface. 700 µL of this solution are carefully applied to each SiO_2 chip with a pipette. The GO adheres to the self assembled adhesive APTES within 1.5 hours of incubation at room temperature. This method is called dropcasting and leads to a stochastic distribution of GO on the surface.

A highly pure GO solution was provided by the University of Bayreuth. This GO has a weight percent of 5% and a little variation in flake size between 20 µm and 50 µm. To get a similar surface coverage with monolayer GO flakes, the solution is diluted to 1:80 with dH_2O. Subsequently dropcasting is performed on the silanized SiO_2 wafers as before.

Reduction of graphene oxide on the chip

The reduction of the GO on the chip can be done with several different methods, already mentioned in Section 2.1.3. The reduction with the carcinogenic hydrazine and the toxic hydriodic acid are described in this section.

The reduction of GO to rGO with hydrazine takes no more preparations and can be performed on the chip's surface. 12 to 14 chips areplaced in the middle of a 26 cm glass petri dish. It is important, that no more than 14 chips are in one petri dish, otherwise the reduction process is less efficient. 1 mL of liquid hydrazine is applied in the corner of the petri dish and not in direct contact with the chips. Right after the application of hydrazine, the petri dish is closed and taped with a high temperature adhesive from 3M to make a vapor barrier. The petri dish is stored in the oven for 16 hours at a temperature of 80 °C to reduce the GO with the vapor

of hydrazine. After this procedure the tape can be removed and the reduction process is finished.

Hydriodic acid (HI) is not carcinogenic and is a more user-friendly reduction method. Up to 20 chips are placed in one petri dish, packed in the middle. The HI is applied directly on top of the SiO_2 surface for the best result of reduction. After covering the lid of the petri dish and closing it with high temperature tape from 3M, it is placed for 16 hours at 80°C in the oven. After the reduction with HI, the chips are washed in deinonized water. Each chip is dipped in two beakers with dH_2O to clean the surface. A final drying procedure of 2 hours in the oven at 130 °C terminates this GO reduction process.

Gold vapor deposition

The application of gold for source and drain electrodes completes the manufacturing of a gFET. The gold vapor deposition is well suitable to get a precise layout of gold electrodes with a drain-source channel width of 40 to 50 µm, a length of 4 mm and a thickness of 70 nm. 25 silicon wafers with an rGO surface are mounted in a holder with a positive metal mask, shown in Fig. 3.1. For a homogenous surface coverage the holder is rotating in the evaporator. The pressure of the evaporator chamber has to be lower than $5e^{-6}$ bar to achieve good results. In the first step 2 nm of chrome are applied to the chip surface and right after 70 nm of gold are evaporated. The vacuum chamber is brought back to atmospheric pressure to remove the chips.

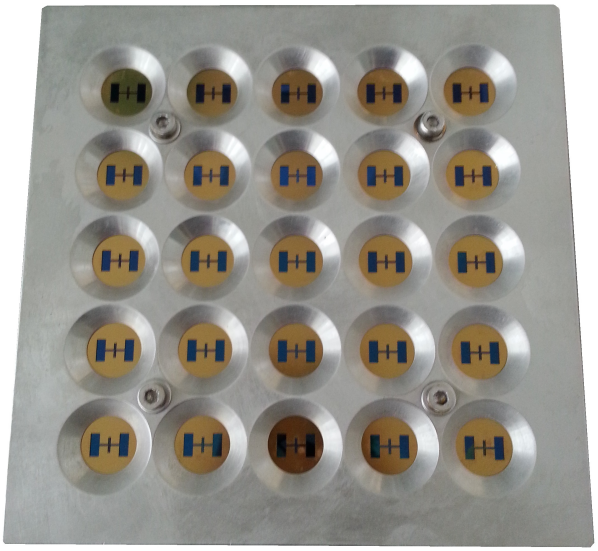

Figure 3.1: Positive gold vapor deposition mask for evaporation of drain and source electrodes on the reduced graphene oxide surface. The drain-source-channel is approximately 50 µm wide and 4 mm long.

Application of protective layers on graphene gFETs

Metal oxides and organic bacterial cell surface layers (S-Layer) are applied to the gFET surface to avoid unspecific binding events with graphene, see Section 2.3.2. The protective layers are an option and do not need to be applied for a working gFET.

Atomic layer deposition ALD

ALD is a thin film deposition technique, used to control the thickness of an applied metal oxide layer. The Institute of Solid State Electronics at the Technical University of Vienna provides ALD for Al_2O_3 and TiO_2 metal oxides. To improve the coating and make it pinhole free, a aluminium seed layer of 3 nm can optionally be applied before. The applied metal oxides are:

- 20 nm Al_2O_3
- 3 nm Al seed layer + 20 nm Al_2O_3
- 30 nm TiO_2
- 3 nm Al seed + 30 nm TiO_2

Sputter coating

Another metal oxide, the Ta_2O_5 was sputtered with an approximate thickness of 20 nm to the gFETs surface using a Leybold Univex 450C.

S-layer application

The Institute for Synthetic Bioarchitectures at the University of Natural Resources and Life Science Vienna provides an application routine for biological S-layer on graphene, who kindly provided the application to the gFET. The layer's thickness is 9 nm [86] and forms a crystalline surface in the drain-source channel.

3.2.4 Functionalization of gFET

To get a biotransducing surface for detecting biomolecules with the gFET, the immobilization of biomolecules is required. The different immobilization methods for proteins on rGO and on metal oxides in the drain-source channel of the gFET are shown. The immobilization of proteins is carried out with linker chemistry.

Immobilization on reduced graphene oxide

A solution of 1 mL tetrahydrofuran (THF) and 1.93 mg of pyrenebutyric acid N-hydroxysuccinimide ester (PBSE) is prepared for a stock solution of 5 mM PBSE linker. After the dilution with THF to a 5 µM PBSE solution, a 10 µL PBSE linker droplet is applied to the drain-source channel on the gFET. The pyrene group of the PBSE linker forms π-π stacks with the graphene surface, while the N-hydroxysuccinimide ester group reacts with amines of proteins to form amides, a covalent bond. The THF evaporates within 5 minutes and proteins can be attached to the surface. OBP9A, OBP9B, OBP14 and Lysozyme are applied as a 20 µL droplet at a concentration of 10 µM on the channel surface. BSA is applied at a concentration of 1 µM. Incubation for 1.5 hours provides protein linking to the gFET. Afterwards, the surface is carefully washed with 17 mM PBS buffer to remove all remnants of PBSE and proteins.

Immobilization on metal oxides

Proteins are connected to metal oxides with (3-Glycidyloxypropyl)trimethoxysilane (GPTMS). The silane connects to the oxides of the metal oxide, while the epoxy group binds to the proteins. The GPTMS is prepared in a 5% solution with pure ethyl alcohol and incubated for 6 hours on the gFET surface. Afther the linker incubation, the gFETs are submerged in pure ethyl alcohol before applying the proteins with the same procedure as described in Section 3.2.4, *Immobilization on graphene*.

Controlling of protein immobilization on metal oxides

Confocal laser scanning fluorescence microscopy, short LSM, is performed to check the protein immobilization on metal oxides Al_2O_3, Ta_2O_5 and TiO_2. According to Kirchberg et al. [87], proteins are labeled with fluoresceine to measure the immobilization of protein cytochrome *c* oxidase (C*c*O) on the metal oxides. Therefore, the proteins are solved in a 17 mM PBS buffer including 0.05% of detergent n-Dodecyl-β-D-maltoside to solubilize the C*c*O. Afterwards, a stock solution of 5-Iodoacetamidofluorescein (IAF) in dimethylsulfoxide using 5 mg/mL is prepared. By adding a tenfold of IAF stock solution to the C*c*O buffer solution and incubated for 1 hour during gently shaking in dark environment, the protein is fluorescence-labeled. The labeled C*c*O proteins are applied to the metal oxides as mentioned in Section 3.2.4, *Immobilization on metal oxide*. The investigation with the LSM is performed with an argon laser with $\lambda_{ex} = 488$ nm and the fluorescence of IAF is detected at $\lambda_{em} = 500$ - 550 nm.

3.3 Measurement set-up

The impedance spectroscopy is utilized to measure the electrical response of the biosensor to different concentrations of ligands in the bulk solution. The measurements are all carried out with a PBS buffer solution, containing concentrations of eugenol of 200 nm, 1 µM, 2 µM, 20 µM, 50 µM, 170 µM and 200 µM. These concentrations were evaluated in a pre-test to determine the lowest and the highest detectable concentration. An MXX low pressure valve (Rheodyne) serves as a switch between the different concentrations, while a peristaltic pump sucks the solution from the probes to the gFET measurement chamber. The gFET is mounted in a flow cell, where two spring contact probes connect drain and source to the potentiostat VMP3 (bio-logic SAS), shown in Fig. 3.3. The gate electrode is the third terminal of the gFET and is connected to the liquid gate on top of the drain-source channel. While the peristaltic pump provides a constant flow of the solution, the low pressure valve changes the solution in programmed time intervals. The measurement set-up is demonstrated in Fig. 3.2. The potentiostat VMP3 is programmed for a impedance spectroscopy measurement from 1 Hz to 500 kHz between drain and source, while a constant gate voltage is applied. The impedance Z is recorded for post-processing and evaluation of binding kinetics.

Figure 3.2: Measurement set-up for detection of analytes in 17mM PBS buffer. From left to right: PBS buffer and solutions with different analyte concentrations, MXX low pressure valve, peristaltic pump for inflow of solution, flowcell with mounted gFET and electrodes, and waste beaker. The potentiostat for electrical measurement is not shown in this picture.

3.3.1 Fluidics

To have a homogenous flow of the solution containing the analyte it is necessary to use a static set-up. Previous works showed, that reproducible results were hard to achieve without a flow cell, so a set-up with a defined liquid channel is used. A peristaltic pump is connected to one side of the channel, while the other side is the outflow of the solution. The gFETs 4 mm long drain-source channel is placed in the flow cell's liquid channel to wash the solution over the biosensing surface.

Flow cell

To measure the response of each gFET in the same environment a defined measurement chamber is required. The liquid channel is seald with a rubber seal and has a length of 18 mm, a width of 2 mm and a height of 2 mm, according to the flow cell developed by Rozman et al. [88]. The gFET is placed in the transparent bottom of the flow cell. The top of the flow cell contains two spring force contact tips for the drain and source connection and a liquid gate electrode in the flow channel. Bottom and top parts are screwed together for stable conditions during the entire measurement. The flow cell's top and bottom are shown in Fig. 3.3. The liquid gate electrode is the tip of a platinum wire with a diameter of 2 mm, coated with a platinum oxide layer. The tip is directly in touch with the solution in the channel.

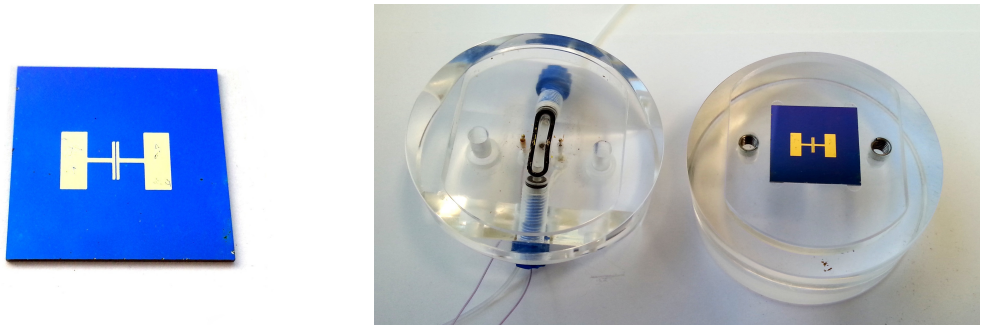

(a) gFET chip (b) Flowcell bottom and top

Figure 3.3: The biosensor platform is demonstrated in (a). The gFETs graphene surface in between the two parallel gold electrodes is the drain-source channel, where the proteins are immobilized. The flow cell with in- and outflow is demonstrated in (b). The top of the flow cell is shown on the left side, with the two gold spring contacts to connect drain and source of the gFET. In the middle of the flow channel is the platinum oxide tip of the gate electrode. The lid is mounted on top for measurements.

Peristaltic pump

The flow rate of the peristaltic pump (ISMATEC) is set to 800 µL/min, while the MXX low pressure valve changes the input channel of solutions with different analyte concentrations, according to the programmed time interval in the Titan MX software. This leads to a constant flow of the solution and reproducible results of the measurements.

3.3.2 Software and electrode configuration of potentiostat

The I_DV_G and I_DV_D curves for characterization of the gFET are measured with the potentiostat VMP3 (Bio-logic SAS). The impedance spectroscopy and cyclic voltammetry (CV) are also performed on this device. For further investigations, the exported files are post-processed in OriginLab 8.5 (OriginLab Corporation). The configurations of the potentiostat's electrodes for all measurements are listed in this section. The gFET is inserted into the flow cell to connect it to the VMP3. The buffer solution and analytes are purged over the biosensor and the flow cell is placed in a Faraday cage during the measurements. The liquid gate electrode is on top of the drain-source channel and is in contact with the aqueous solution.

I_DV_G curve

The I_DV_G curves of the gFET are measured with the VMP3 (Bio-Logic SAS). The gFET is placed in the flow cell and the electrodes are configured as shown in Section 3.3.3. The drain-source voltage V_D is set to 500 mV at the maximum to avoid damage of the graphene surface and the gate voltage V_G is gradually increased from -1 V to +1 V with the *LSV* setting. ΔV_G is set to 20 mV per second to achieve a high resolution for the I_DV_G curve. The *PPI* setting is employed to measure the drain-source current I_D on the VMP3. The EC-Lab (Bio-Logic SAS) software settings are shown in Fig. 3.4.

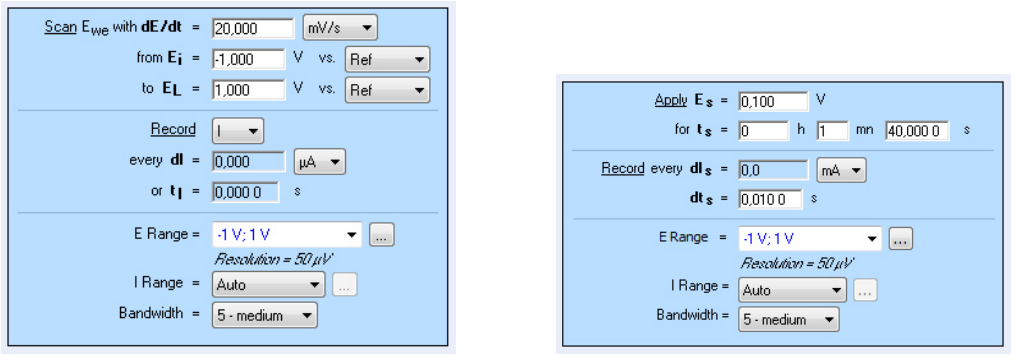

(a) LSV - Gate settings

(b) PPI - $I_D V_G$ drain-source settings

Figure 3.4: Settings in the EC-Lab software (Bio-Logic SAS) to perform the $I_D V_G$ measurement.

$I_D V_D$ curve

The $I_D V_D$ curves of gFETs are measured in the flow cell, with connected drain and source to one channel of the VMP3. The gate electrode is not required for this measurement. All electrode configurations are shown in Section 3.3.3. To acquire the drain current I_D while the drain-source potential V_D increases, the setting *LSV* is employed in the EC-Lab software. The voltage V_D increases with $\Delta V_D = 20$ mV per second from -600 mV to +600 mV. Further EC-Lab software settings are shown in Fig. 3.5 (a).

Cyclic voltammetry

The cyclic voltammetry was applied to measure the passivation of the protective layer on top of the graphene. As a reference, also the the rGO gFET was measured with this method. The protective layer should prevent the redox reaction of the probe [89]. Therefore, one electrode of the gFET was applied to the working electrode of VMP3, while a platinum wire was connected to the VMP3s counter and reference electrode. The electrode configuration for CV is shown in Section 3.3.4. A 100 mL droplet of potassium ferricyanide was applied on top of the protective layer and the platin wire was plunged into the solution. The VMP3 was set to *CV* and the voltage was linearly increased from -1.2 V to +1.2 V and back again to get a full cycle. The lower the redox reaction current in the CV plot is, the better the passivation of the protective layer is. The detailed settings for the CV are listed in Fig. 3.5 (b).

Impedance spectroscopy

The impedance spectroscopy of the gFET is performed with the flow cell while different analytes are purged over the biosensor. The electrode configuration for impedance measurement with the VMP3 (Bio-Logic SAS) is shown in Section 3.3.3. The gate voltage is set to a constant potential with the EC-Lab setting *CA*. A sinusoidal drain-source voltage with frequencies from 1 Hz to 500 kHz is applied to the drain-source channel, carried out by the EC-Lab setting *PEIS*. The EC-Lab software measures the magnitude of the current I_D and its phase shift φ in respect to the drain-source voltage. The calculated $|Z|$ and phase shift φ are recorded for each frequency. A

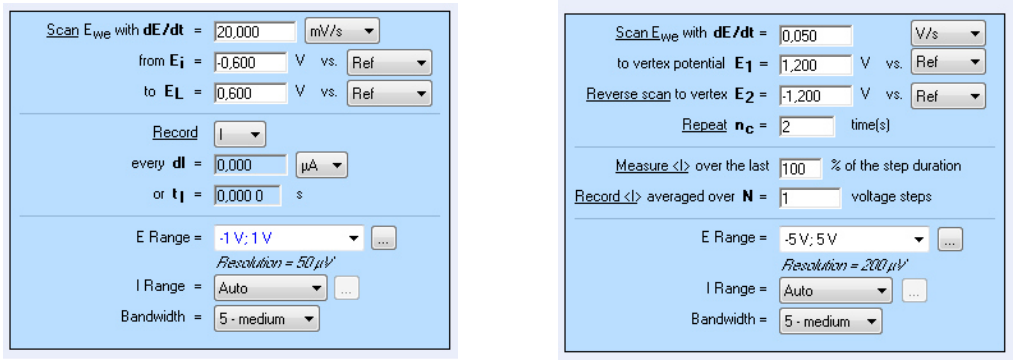

(a) LSV - I_DV_D drain-source settings

(b) CV - CV settings

Figure 3.5: In (a) the settings of EC-Lab software (Bio-Logic SAS) to perform a I_DV_D measurement. The settings to perform cyclic voltammetry measurements are shown in (b).

frequency sweep from 1 Hz to 500 kHz ($\Delta f = 10$/decade) is performed, according to the software settings, shown in Fig. 3.6.

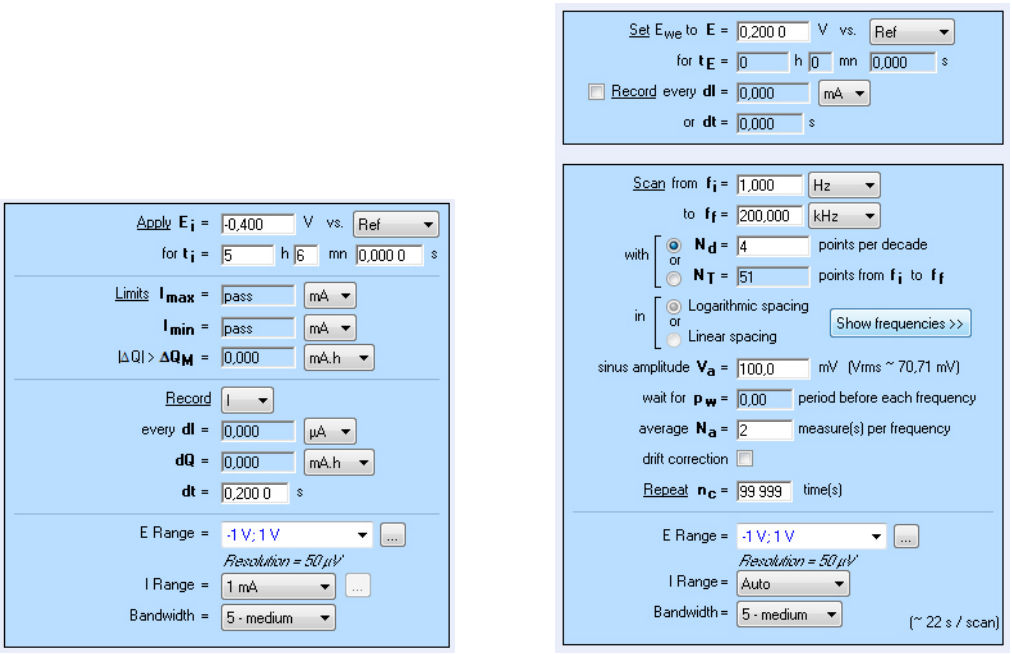

(a) CA - Gate settings

(b) PEIS - Drain-source settings

Figure 3.6: Settings in the EC-Lab software (Bio-Logic SAS) to perform the impedance spectroscopy measurement.

3.3.3 I_DV_G and I_DV_D and impedance spectroscopy electrode set-up

Drain and source of the gFET are connected to channel 1 of the potentiostat:

- **DRAIN electrode:** Channel 1 *CE*, *REF1* and *REF3*
- **SOURCE electrode:** Channel 1 *GND* and *REF2*

The source electrode is connected to ground and the housing of the Faraday cage.

To measure the I_DV_G curve and impedance spectroscopy, the gate electrode of the gFET is connected to channel 2 to control the gate voltage:

- **GATE electrode:** Channel 2 *CE*, *REF1* and *REF3*
- **GND electrode:** Channel 2 *GND* and *REF2*

The GND electrode is connected to ground and the housing of the Faraday cage. The working mode *CE to GND* is chosen in the software settings for channel 1 and 2.

3.3.4 Cyclic voltammetry electrode set-up

For the CV measurement one channel of the potentiostat is required.

- **Gold electrode:** Channel 1 *REF1*
- **Platinum wire:** Channel 1 *CE* and *REF2*

The working mode *CE to GND* is chosen in the software settings for channel 1.

3.4 Characterization of gFETs

For post processing of the acquired data, the equations in this section are employed. The measurements are all evaluated in OriginLab 8.5, including all plots and fits, listed in Chapter 4.

Electron mobility

To calculate the electron, respectively the hole mobility of the produced rGO field-effect transistors, the slope of the I_DV_G curves was employed. Therefore the linear regime of the I_DV_G was fitted by a line, giving the results of intercept and slope. The resulting slope m_{lin} is given in A/V. Equation (3.1) describes the correlation between the linear fit m_{lin} (I/V), the mechanical properties of the gFETs width W (m) and length L (m) of the graphene gap, the drain-source voltage V_D (V) and the gate insulator capacity C_i [90].

$$\mu = L/W \cdot 1/V_D \cdot 1/C_i \cdot m_{lin} \tag{3.1}$$

The result of this equation is the electron, respectively the hole mobility μ (cm^2/Vs). If the slope of m_{lin} is negative, then the mobility of the electron holes, or traps can be calculated.

3.4.1 Binding kinetics

The exponential fits for the binding kinetics are performed in OriginLab, resulting in k_{obs}. All k_{obs} are plotted against the concentrations to get the linear fit. The linear fit contains k_{on} and k_{off} and they are calculated with equation (2.11). K_D and K_A are determined with equations (2.6) and (2.7) and the Langmuir fit is performed with equation (2.10) in OriginLab.

4 Results and Discussion

4.1 Graphene characterization

The basis of a properly working gFET is the graphene, respectively the reduced graphene oxide (rGO). The first verification of the gFETs applicability is a resistance measurement between the drain and source electrodes using an ohmmeter. After a successful reduction of the graphene oxide, the resistance is below 1 kohm. To investigate the SiO_2 wafer for rGO surface coverage and to see the results of the reduction process, optical methods were employed.

4.1.1 Surface coverage

Scanning electron microscopy

To investigate on the rGO surface coverage on the SiO_2 wafer, scanning electron microscopy (SEM) was employed. In Fig. 4.1 the coverage of AIT synthesized rGO is shown at two different magnifications.

A good rGO junction between the drain and the source electrode was achieved as the resulting surface coverage was greater than 80%. For the AIT synthesized rGO it can be noticed, that some undesired material is within the probe, shown in Fig. 4.1. Impurities were found in the probe of the AIT synthesized rGO, see Fig. 4.1. These may originate from the synthesis process and are unavoidable. However for the prototypes of gFETs these impurities are of no consequence as the material is not conductive. Impurities in the rGO/dH_2O solution could be removed by using ultrafiltration. After producing useable gFETs with this rGO, a more pure and stable GO solution was ordered from the University in Bayreuth. After optimization of the solution's dilution, the surface coverage was again greater than 80%, but showed no impurities on the SiO_2 wafer surface after reduction.

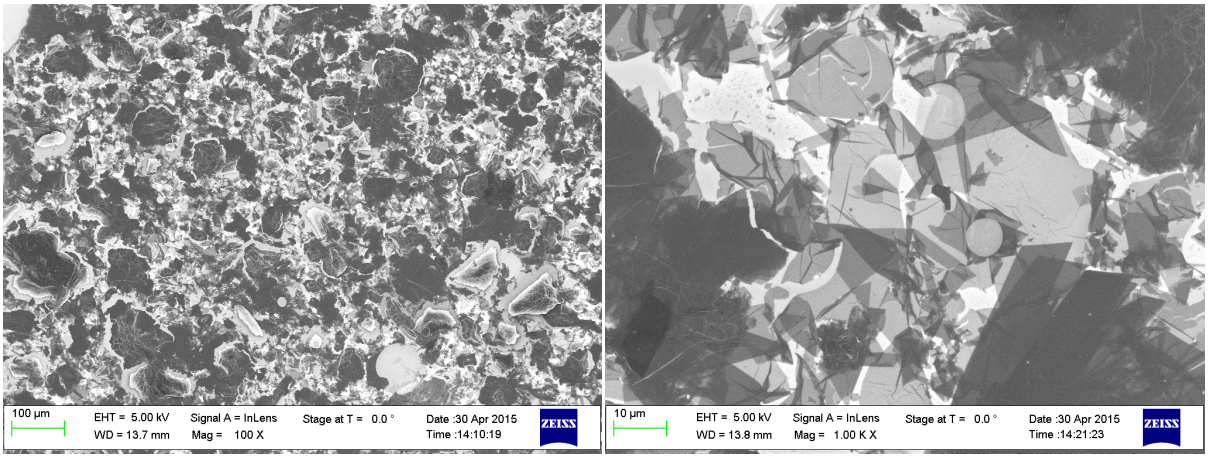

(a) rGO (b) rGO

Figure 4.1: Surface coverage of rGO on SiO_2 wafer. The AIT synthesized reduced graphene oxide on SiO_2 chip surface is shown in (a) and (b). Magnifications were 100x and 1.000x. Pictures taken with scanning electron microscope

Reflected light microscopy

Reflected light microscopy can be used for a quick lab investigation on the surface during the manufacturing process. The graphene layers can be seen on the 300 nm thick SiO_2 layer in Fig. 4.2.

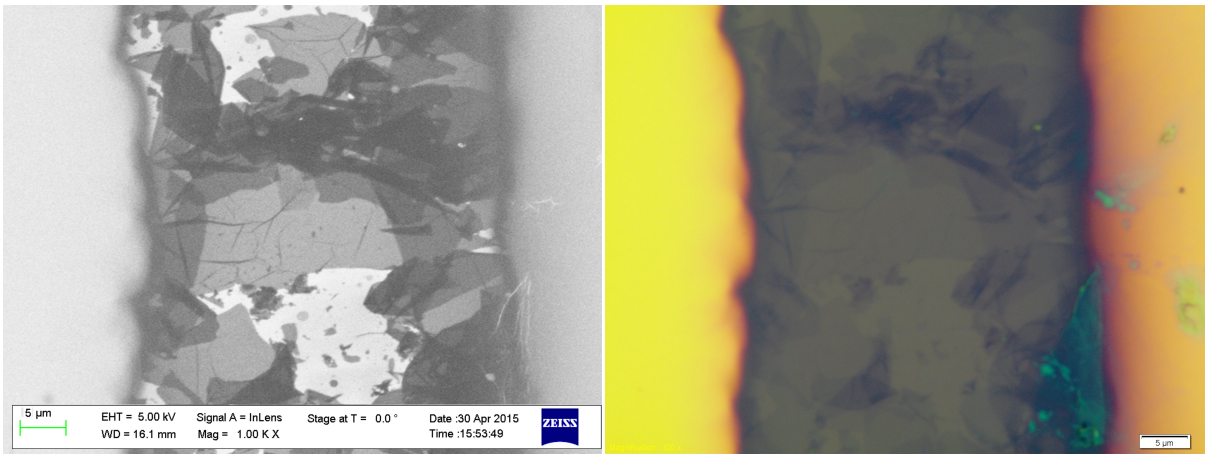

(a) SEM picture of gFET gap (b) light microscopy

Figure 4.2: Comparison of SEM picture and reflected light microscopy of the same spot of a gFET. In (a) the rGO junction of several flakes between drain and source electrode can be seen. The image was taken with SEM. The reflected light microscopy image in (b) shows exactly the same position, but with reflected light microscopy.

As expected the contrast in reflected light microscopy images is lower compared to SEM images, but they can be used to confirm the presence of the rGO on the gFET. It is an inexpensive alternative to an investigation with SEM, but it is only applicable if some conditions are met, i.e. The Si wafer material must have a 300nm thick SiO_2 layer. If this value is lower, a monolayer of rGO flakes will no longer be distinguishable from the background and hence no contrast will be seen. With a correct surface and light set-up, a trained eye is able to see single flakes and

can tell the quality of the produced rGO for gFETs with reflected light microscopy [91].

4.1.2 Comparison of graphene oxide and reduced graphene oxide

At the beginning of the gFET fabrication the graphene oxide (GO) was applied on the SiO_2 surface by drop casting. To remove the oxygen-containing groups of graphene oxide, it is necessary to reduce the sp^3 hybridized GO to the so called sp^2 hybridized reduced graphene oxide (rGO). The reduction of the AIT synthesized GO was carried out using hydrazine, whereas the reduction of the Bayreuth GO was done using hydriotic acid. As the GO is an insulator, the measured resistance is above the scale of the used Fluke multimeter. After the reduction process, the resistance of the gFETs was in the range of 100 Ohm to 5 kOhm. This showed that both the reduction process and the sp^2 hybridization had taken place correctly. The optical analysis of the GO before and after reduction are shown in Fig. 4.3. Here hydriotic acid (HI) reduction of Bayreuth GO is shown.

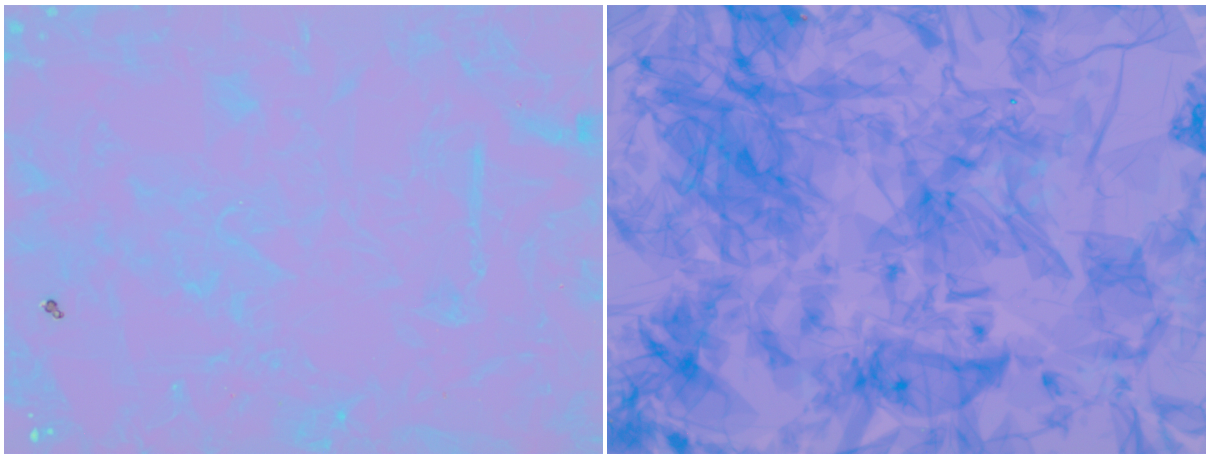

(a) graphene oxide (b) reduced graphene oxide

Figure 4.3: Comparison of graphene oxide to reduced graphene oxide. Hydriodic acid was used to reduce Bayreuth GO within 12 hours at 300°C.
Images were taken with reflected light microscopy

In Fig. 4.3 (a) the transmission of GO is about 99%, so there is almost no graphene visible. After reduction to rGO, a significant decrease of transmission can be noticed, demonstrated in Fig. 4.3 (b).

The decrease in resistance value below 5 kOhm combined with changes in the visible light transmission lead to the conclusion that the applied reduction methods are well suited for the production of rGO, and can therefore be used to produce gFETs.

4.2 $I_D V_G$ characteristics of gFET

The $I_D V_G$ curve of a field-effect transistor shows its drain-source current behavior at ramped gate voltage sweeps. Therefore, the conductivity of a gFET's drain-source channel is controlled by an external electric field, induced by the gate voltage. In Fig. 4.4 the dependency of I_D on

the electric field, respectively the gate voltage V_G is shown.

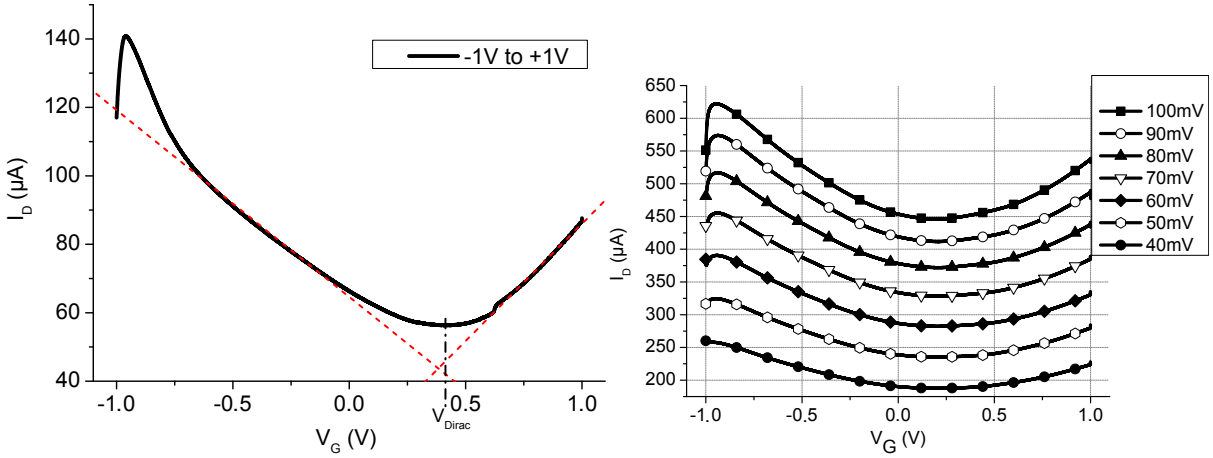

(a) $I_D V_G$ of rGO gFET

(b) $I_D V_G$ at different V_{DS}

Figure 4.4: Measured $I_D V_G$ curves of the developed rGO gFET. I_D was measured while the gate voltage V_G varied from -1 V to +1 V, shown in (a). The dependency of the $I_D V_G$ curve to different drain-source voltages V_D is presented in (b). All measurements were done on gFETs with rGO surface. The measured resistance of the gFET shown in (a) is 600 ohm and of the gFET in (b) is 230 ohm.

The resulting $I_D V_G$ curve reflects the ambipolar behavior of graphene in dependency on electric fields [14]. The negative slope of the linear fit (red dashed line) can be used to calculate the hole mobility, while the positive slope above the neutral point for the electron mobility. With equation (3.1) the hole and electron mobilities were calculated and are listed in Tab. 4.4. The ambipolar properties of graphene lead to a gFET with an n-type behaviour in the negative range of V_G and a p-type in the positive range. The neutral point is found at the gate voltage, where the graphene's conductivity, therefore I_D, has its minimum. This point was found for all produced gFETs between V_G 0.2 V and 0.4 V and is called the Dirac-point. With these properties it is possible to have an n-type or a p-type gFET by adjusting V_G between -1 V and +1 V.

4.2.1 $I_D V_D$ characteristic of gFET

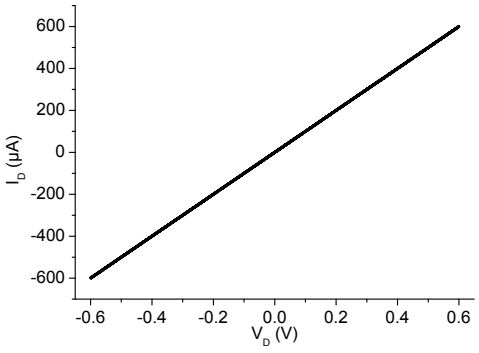

Figure 4.5: $I_D V_D$ of rGO gFET

The $I_D V_D$ characteristics were measured for further characterization of the gFET. In Fig. 4.5 the drain-source current I_D is linearly dependent on the applied drain-source voltage V_D. The gFET had a measured resistance of 1 kOhm and during the measurement the gate voltage was set to zero. The range of V_D was -600 mV to +600 mV. Higher voltage ranges (-5 V to +5 V) were also measured, but the resulting $I_D V_D$ curve is still linear. In the measured regime, the saturation of I_D could not be reached. This is due to the non-existing bandgap and so the synthesized rGO behaves like a metallic conductor [92]. The saturation is reached for high V_D. The

gFET, shown in figure Fig. 4.5, behaves like an ohmic resistor.

4.3 pH dependency of gFET

The dependency of the drain-source current I_D on the pH value of the liquid solution was studied. Here the gate voltage V_G was set to -400 mV and V_D to 50mV. The impedance spectroscopy from 1 Hz to 500 kHz was performed and the results are shown in Fig. 4.6. For a better demonstration, the frequencies 1 kHz, 10 kHz and 100 kHz at different pH values are plotted separately. PBS buffer with 17 mM ionic strength and pH values from 4.5 to 8.5 were washed over the gFET. The change of magnitude |Z| and phase(Z) according to the pH values are shown in Fig. 4.6 (a) and Fig. 4.6 (b).

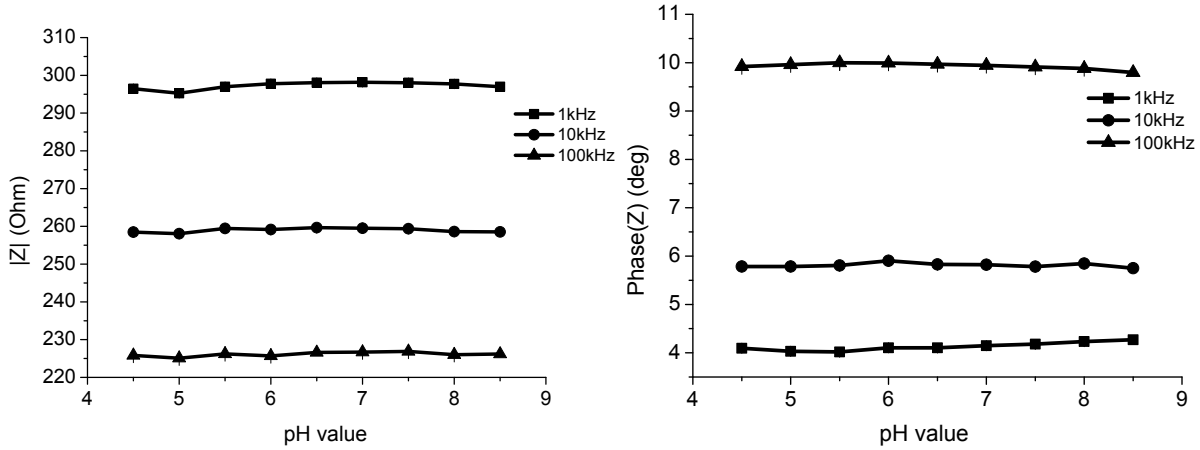

(a) |Z| vs. pH (b) φ vs. pH

Figure 4.6: Dependency of |Z| and φ to pH value changes at three different frequencies, 1 kHz, 10 kHz and 100 kHz

It can be seen, that neither the magnitude |Z|, nor the phase angle of Z are influenced by the change of pH value. For all further measurements, the preparation of probes was monitored with a pH-meter with the precision of ±0.01. Therefore, it can be said, that this sensor is not dependent on minor changes of pH values.

4.4 Ionic strength dependency of gFET

To have a stable measurement set-up, a pH value buffered solution is necessary. In all experiments a PBS buffer with a maximum concentration of 170 mM was used. For enhancement of the response signal, the electrolytic solution was diluted to a minimum concentration of 17 mM, see Section 2.3.3. The measurements of gFET's response to different PBS buffer concentrations, respectively ion concentrations are shown in Fig. 4.7. The Bode plot for |Z| and phase(Z) at a frequency range of 1 Hz to 500 kHz is plotted. The measurements were performed with different concentrations of the PBS buffer with ionic strenghts ranging from 21 mM to 170 mM.

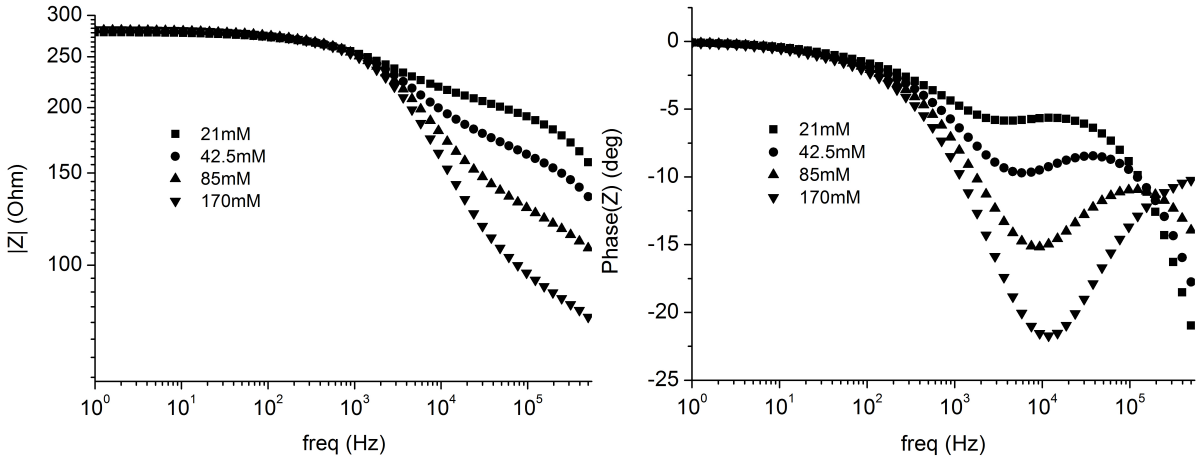

(a) |Z| vs. ion concentrations

(b) Phase(Z) vs. ion concentrations

Figure 4.7: (a) shows the gFETs magnitude |Z| and (b) the phase(Z), depending on different ionic concentrations of the PBS buffer. The ionic liquid is washed over the rGO between the drain-source gap with a liquid gate electrode on top.

As shown in Fig. 4.7 (a) and (b), the gFETs magnitude |Z| and phase(Z) are highly dependent on different ionic concentrations of the solvent in the higher frequency regime. The dependency can be exponentially fitted and is shown in Fig. 4.8.

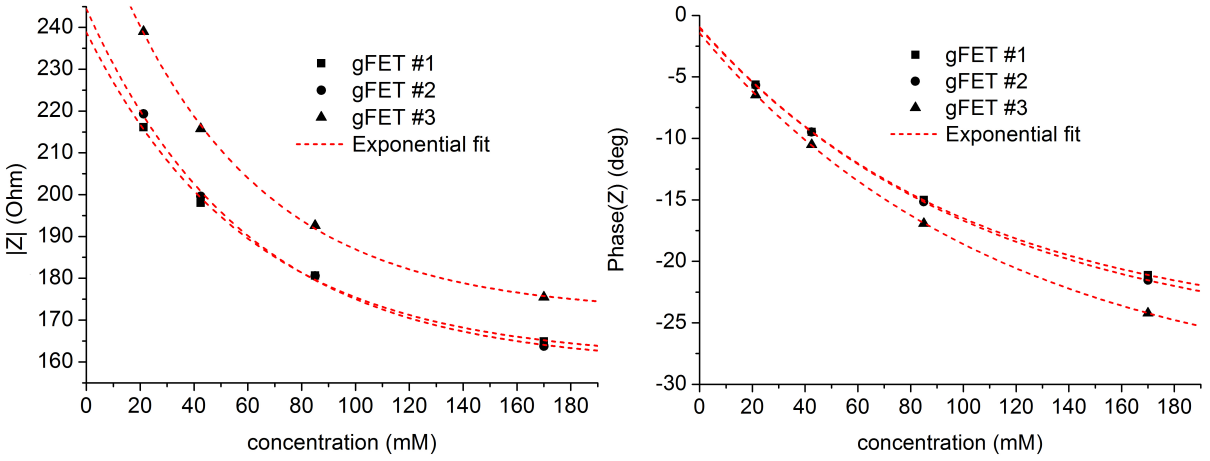

(a) |Z| at 10 kHz

(b) Phase(Z) at 10 kHz

Figure 4.8: Three different gFETs with resistances of 210 ohm, 270 ohm and 300 ohm were measured with different ionic liquid concentrations. The highest dependency on ionic changes appears for phase(Z) at 10 kHz. The measured magnitude |Z| and phase(Z) at 10 kHz are shown in (a) and (b) for all three gFETs at different ionic buffer concentrations. The measurements can be fitted exponentially (red dashed lines).

The exponential fit for ionic changes can be performed for all frequencies, starting above 1 kHz. There is only little change in magnitude and phase(Z) at frequencies below 1 kHz.

4.4.1 Electrical equivalent circuit

The group of Misra et al. presented an abstracted electrical equivalent circuit, short EEC, of a field-effect transistor under the influence of ionic fluids [93]. Applied to the produced rGO FET,

an EEC as an abstracted version of the real system was derived. Fig. 4.9 (b) shows the EEC, created according to the physical construction of the gFET and the aqueous solution.

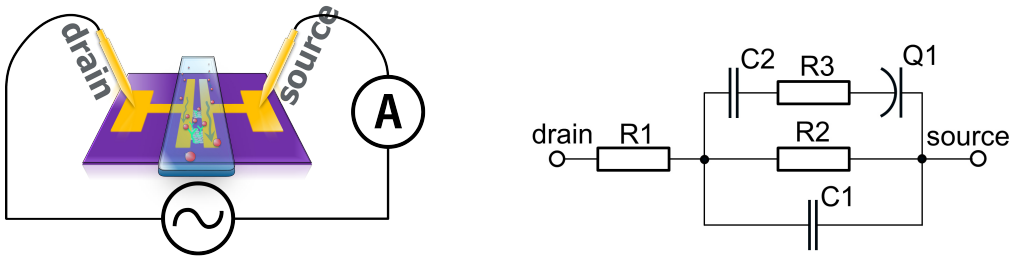

(a) Real gFET system (b) EEC of gFET

Figure 4.9: The two figures show the present gFET and the derived electrically equivalent circuit (EEC). In (a) the produced gFET and its connection pads are shown. Here the gate electrode was removed to improve the visibility on the drain-source gap with the ionic liquid washed over it. (b) shows the most simplified EEC to simulate the magnitude $|Z|$ and phase(Z) for ionic liquids with different ion concentrations on top of the sensitive area of the gFET.

The EEC represents the components of the developed gFET and the ionic liquid. It can be seen as a combination of contacts and wires, interfacial area and bulk media [80]. In Tab. 4.1, the representations of all electric components are listed.

Electrically equivalent circuit		
Component	Equivalent Element	Represents
Resistor	R1	wire and spring tip resistance
Capacitor	C1	capacitance of two parallel electrodes
Resistor	R2	graphene surface resistance
Capacitor	C2	ionic interface capacitance
Resistor	R3	transfer resistance at the ionic interface
Constant phase element	Q1	non-linear double-layer charge transfer

Table 4.1: Components of electrically equivalent circuit to represent the real gFET system.

Contacts and wires

The resistor R1 represents the resistance of the spring tips to contact the gFETs drain and source pads in the flow cell, including all wires and contact resistances. Therefore R1 remains almost constant during the entire measurement.

Interfacial area

The gFETs geometrical arrangement affects the capacity C1 between the two working electrodes of drain and source. The parallel electrodes lead to a frequency depending capacitance, even without any bulk solution on top.
The resistor R2 represents the graphene layer, connecting drain and source. This is simplified as an ohmic resistor and is a frequency independent component.

Bulk media

The ionic liquid is represented by the resistor R3 and the capacity C2. Since the conductance and capacitance of the ionic liquid changes with concentrations of ions, these components mostly influence the circuit's impedance. The constant phase element Q1 represents the non-linear double-layer capacitive charging effects, and represents the junction between the conductive area of the gFET, graphene and the gold electrodes, and the ionic bulk solution [80].

The impedance Z of the derived electrically equivalent circuit can be expressed with equation (4.1) and representation by the components in equation (4.2),

$$Z_{EEC} = Z_{R1} + \frac{1}{\frac{1}{Z_{C1}} + \frac{1}{Z_{R2}} + \frac{1}{Z_{C2}+Z_{R3}+Z_{Q1}}} \tag{4.1}$$

$$Z_{EEC} = R1 + \frac{1}{j\omega C1 + \frac{1}{R2} + \frac{1}{\frac{1}{j\omega C2}+R3+\frac{1}{Q1(j\omega)^a}}} \tag{4.2}$$

With the simulation tool *Z Fit*, part of the program *EC-Lab*, the values for the components were calculated. Tab. 4.2 shows the parameters which were identified from the measured data. With these component values, the response of the gFET to different ionic concentrations of the PBS buffer can be simulated. In Fig. 4.10, the measured and calculated impedance Z is shown. Z is represented as the magnitude |Z| and the phase(Z).

Values of EEC components					
Component	Unit	21mM	42.5mM	85mM	170mM
R1	Ohm	65	71.6	73	68
C1	nF	1.66	2.33	4.36	13.06
R2	Ohm	246	240	238	243
C2	μF	0.337	0.452	0.783	4.04
R3	Ohm	266	148	68	32
Q1	μF $cm^{-2}s^{(a-1)}$	21.4	9.19	3.56	1.49
α	1	0.454	0.570	0.675	0.751

Table 4.2: All components of EEC in different ionic liquid concentrations. The values of all fitting parameters were calculated with the fitting tool Z fit.

With the EEC model it is possible to discriminate the influence of ionic concentrations from other surface reactions, such as unspecific or protein binding kinetics. To prove the plausibility of the fitted data, close examination of each component value is required. This is necessary to prove that the simulation follows the expected behavior due to ion concentration changes in the ionic liquid. As expected, the value for resistor R1, contact and wire resistance, remains constant at all ion concentrations. The rGO resistance R2 should also stay constant, independent of the electrolyte on top of the sensitive gap. Since the dielectric liquid increases its conductivity with increasing numbers of ions, the resistor R3 is getting smaller. It can be noticed, that

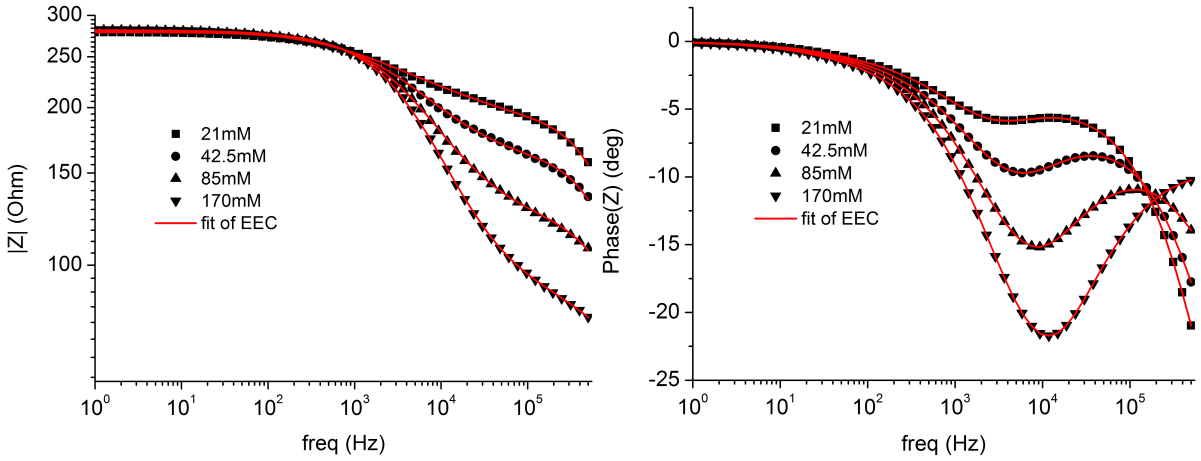

(a) |Z| measured and simulated

(b) Phase(Z) measured and simulated

Figure 4.10: (a) and (b) show the results of the measured data for |Z| and phase(Z) (black symbols) and the fitting curves of the simulated data (red line). The ion concentration of the PBS buffer was changed during the measurement from 21 mM to 170 mM.

the resistance R3 approximately halves with the double ion concentration. With increasing ion concentration, the capacities C1 and C2 also increase, due to the free charges and therefore higher electric double layer capacity C_{EDL} [94].

The constant phase element Q1 decreases whilst the exponent α increases. If α equals 1, Q1 would represent a perfect capacitor, whereas decreasing α to 0 would make Q1 a perfect resistor. Meaning, Q1 is turning into a capacitor with high ion concentrations due to complete vanishing of the resistance part. C2 represents the ideal Q1, respectively the electric double layer capacitance C_{EDL}, for high ionic concentrations.

All these single component analysis fulfill the expectations, so the EEC can be seen as a good approach for simulation of different ion concentrations on the present system. With the EEC a simulation for the gFET's response to different ion concentrations can be performed. With a predicted value at a certain concentration, a measurement can be validated and corrected if necessary.

4.5 Functionalization of the gFET

In this section the response of gFETs with immobilized OBP14 is demonstrated. The presence of eugenol in the PBS buffer solution changes the electrical properties of the gFET due to its functionalization. Proteins like odorant binding protein 14, anti-bovine serum albumin, lysozyme and odorant binding protein 9A and 9B where immobilized on the rGO surface in the gap between drain and source using a linking molecule. Impedance spectroscopy was performed to measure the response of the gFET to different ligands.

4.5.1 OBP14 immobilized on gFET to measure eugenol binding kinetics

Fig. 4.11 shows the response of two different gFETs to eugenol and BSA titration. Both gFETs were produced in the same way, but only one was functionalized with OBP14 on the rGO surface. This protein is known to bind eugenol on its binding site. In Fig. 4.11 (a) the normalized magnitude |Z| of both gFETs at 1 Hz is plotted. The response at a frequency of 1 Hz was chosen, because here the gFETs showed their maximum signal to noise ratio. Both gFETs were first washed with 17 mM PBS buffer and then a eugenol titration with concentrations from 200 nM to 200 μM in PBS buffer was performed. After washing the gFETs with 17 mM PBS buffer again, the titration with bovine serum albumin (BSA) was performed. For reasons of comparison, all magnitudes were normalized to their baseline levels at PBS buffer washing immediately before the ligand titration.

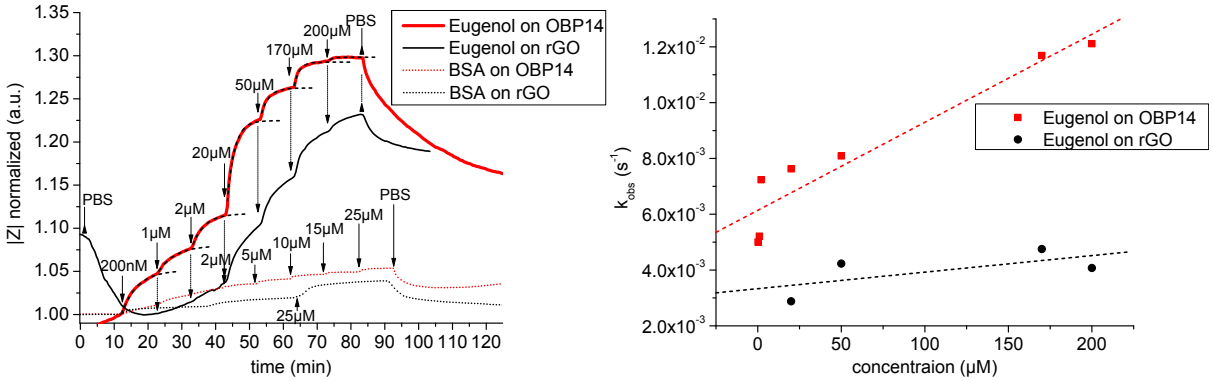

(a) Comparison of blank rGO and OBP14 gFET

(b) k_{obs} of blank and functionalized gFET

Figure 4.11: Titration of eugenol and BSA on two different gFETs. One gFET has immobilized odorant binding protein 14 (OBP14) on rGO, while the other has the blank rGO surface. The response of the gFETs is demonstrated as the change of magnitude |Z|. (a) shows the gFETs response |Z| with and without immobilized OPB14 to eugenol and to BSA and (b) demonstrates the calculated value for k_{obs} of binding kinetics.

The OBP14 gFET shows a higher response in magnitude |Z| compared to the blank rGO gFET. This is due to selective binding of eugenol to the protein binding sites. Those binding sites are highly selective and lead to conformational changes of the protein, which change the location of charges on the graphene surface. If the ligand (eugenol) is captured by the protein (OBP14), the magnitude |Z| increases. The impedance of the frequency spectrum from 1 Hz to 500 kHz was measured, the maximum of response still happened in the lower frequency range from 1 Hz to 100 Hz. Thus, the selected frequency for the response was 1 Hz to compare the blank rGO gFET with the functionalized gFET. The specific response is higher due to its specific OBP14 kinetics, but still, the unspecific bindings to the rGO surface is not negligible. The change in magnitude |Z| of a blank rGO gFET could be explained by studying the structure of eugenol, as shown in Fig. 4.13. In Section 4.5.1, these aromatic structures binding events to rGO are further discussed. In Fig. 4.11 it should also be pointed out that whereas OBP14 gFET responds at 200nM eugenol, the rGO gFET shows no reaction.

It can also be observed that the response signal of the BSA titration is very low compared to the response to eugenol. This is due to the non-aromatic structure of the bovine serum albumin and its low affinities to the OBP14 protein. The binding kinetics of BSA are significantly different

to eugenol, so BSA can be easily distinguished from specific kinetics of eugenol to OBP14.

For further analysis of the binding kinetics, exponential fits of the |Z| responses were performed. The observed time parameter k_{obs} (s^{-1}) of the exponential fit represents the binding affinity to the protein of a ligand at a certain concentration. In Fig. 4.11 (b) the resulting time constants are plotted versus the corresponding concentrations. Every concentration establishes another equilibrium with the protein, respectively to the rGO surface and so the k_{obs} change with every ligand concentration. The slope of the fitted curve (red dashed line) follows the linear equation (4.3),

$$k_{obs} = k_{on} \cdot c + k_{off} \tag{4.3}$$

where k_{on} represents the slope of k_{obs} and has the unit $M^{-1}s^{-1}$, c is the concentration in M and k_{off} is the intercept in s^{-1}, see also Section 2.3.4. The linear fit in Fig. 4.11(b) shows, that the gFET with immobilized OPB14 shows a higher binding constant with increasing eugenol concentration, further proving specific binding at this point. The measured and calculated values for all k_{on} and k_{off} are listed in Tab. 4.5.

Langmuir adsorption isotherm binding kinetics

To determine the surface coverage of an analyte, here the ligand on the immobilized protein, the Langmuir adsorption model can be applied [95] [96], see also Section 2.3.4. By plotting the saturation level of |Z| for each concentration, the coverage can be shown and the Langmuir adsorption model can be fitted in Fig. 4.12 with the function (4.4),

$$\theta = \frac{c \cdot K_A}{1 + c \cdot K_A} \tag{4.4}$$

where c is the concentration in M, K_A the association constant in M^{-1} and θ the surface coverage, ranging from 0 to 1 [97]. The bias level of magnitude |Z| at zero ligand concentration represents a surface coverage of zero. This leads to the assumption, that 100% surface coverage is reached, when an increase of ligand concentration does not lead to an increase of |Z|, because all binding sites already formed a complex with the ligand. To represent |Z| as the surface coverage θ, it has to be compressed to a range between 0 and 1, where 0 equals the value of |Z| where there is no ligand affinity and 1 is the maximum achievable |Z| due to analyte binding.

In Fig. 4.12 the dissociation constant K_D can be directly read at 50% of the complete surface coverage. The K_D is 3.1 μM. The measured K_D corresponds with the upper limit of the results of odorant binding protein researchers, who evaluated the dissociation constant in a range between 90 nM and 3 μM [98]. The titration was performed in the range from 200 nM to 200 μM and the Langmuir adsorption isotherm shows that the surface coverage at 200 μM has reached its maximum, i.e. if the concentration increases, the response Z would not increase any further and hence the protein surface would be saturated. Regarding the Langmuir fit, the limit of detection is lower than 200 nM, but the gFET was not tested for lower eugenol concentrations.

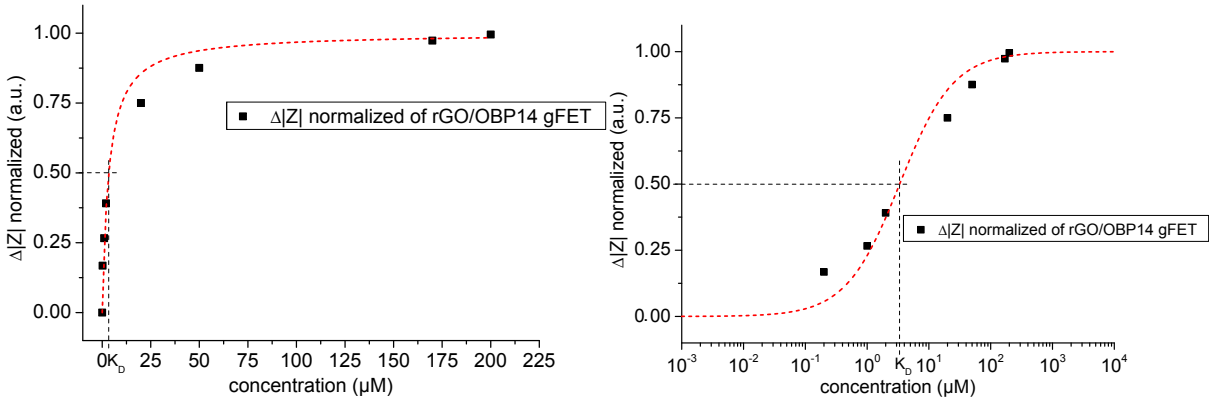

(a) Linear Langmuir isotherm

(b) Logarithmic Langmuir isotherm

Figure 4.12: Langmuir adsorption isotherm binding kinetics fitted to represent the magnitude |Z| as surface coverage. In (a) the Langmuir fit was applied to the linear |Z| dependency to the ligand concentration. (b) shows the logarithmic dependency.

Unspecific binding kinetics of eugenol to graphene

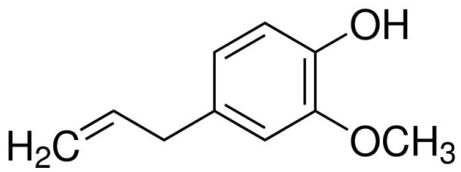

Figure 4.13: Chemical structure eugenol

π-π stacking of aromatic rings on the graphene surface could account for the undesired blank rGO |Z| response. Benzene rings, which are six carbon atoms in an aromatic structure, have a configuration similar to that of graphene and may lead to an unspecific binding to the graphene surface. The group of Hanke et al. of the Surface Research Center and Department of Chemistry showed the interactions and adsorption of aromatic systems on graphene through π-π stacking [99]. They showed, that the adsorption energy is a complex combination of different mechanisms, such as dispersive and electrostatic interactions. A simplified model for calculation of the binding energy E_{bind} was derived in equation (4.5),

$$E_{bind} = N_C E_{CC} + N_H(E_{CH} - E_{CC}) \tag{4.5}$$

where E_{CC} is their fitted energy per graphene-like carbon and E_{CH} is their fitted energy per benzene-like carbon. N_H and N_C are the numbers of hydrogen and carbon atoms respectively. For graphene-like and benzene-like carbon atoms they estimated $E_{CC} = 49.2$meV/atom and $E_{CH} = 80.1$meV/atom and so E_{bind} can be simply calculated by counting N_H and N_C. For eugenol $C_{10}H_{12}O_2$ this would yield to $N_H = 12$ and $N_C = 10$. Applied to equation 4.5 the result for $E_{bind} = 862.8$meV for eugenol to graphene.

To avoid unspecific bindings on the rGO surface, a protective layer could be applied. A certain distance between rGO and the ligands in solution may reduce the binding energy and therefore reduce unspecific response. The results for metal oxide and protein surface protective layers are shown in Section 4.6

4.5.2 Responses of Lysozyme, Anti-BSA, OBP9A and OBP9B to eugenol

Fig. 4.14 shows the gFETs response |Z| to eugenol when other proteins than OBP14 are immobilized. Those proteins have no specific binding affinities to eugenol.

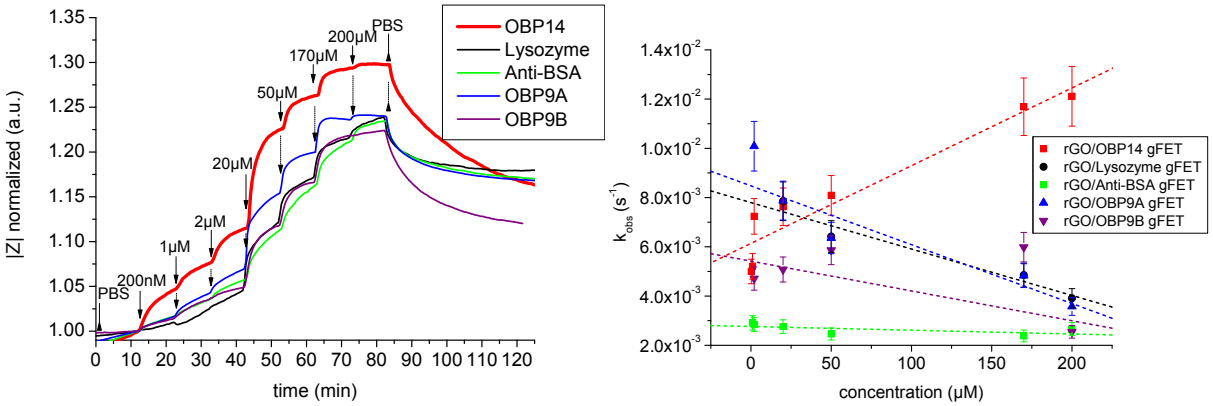

(a) Comparison of immobilized OBP14 with other proteins on gFET

(b) k_{obs} of unspecific and specific bindings

Figure 4.14: Titration of eugenol on gFETs with different immobilized proteins. For specific binding kinetics, OBP14 was immobilized. For observation of unspecific binding kinetics, the gFET was functionalized with the proteins Lysozyme, Anti-BSA, OPB9A and OBP9B. (a) demonstrates the response of |Z| at 1 Hz and in (b) the k_{obs} of all kinds of proteins is plotted versus concentrations.

The OBP14 shows the highest change in magnitude |Z| to eugenol titration compared to the other proteins immobilized on the graphene surface as seen in Fig. 4.14 (a). The response at concentrations as low as 200nM of eugenol is significant and an exponential fit for binding kinetic calculations can be performed. Fig. 4.14 (a) shows, that the magnitude |Z| of all gFETs follows the concentration of eugenol. The proteins Lysozyme, Anti-BSA and OBP9A/B also respond to different eugenol concentrations, however the binding kinetics reveal the binding affinities of unspecific binding. Fig. 4.14 (b) shows the k_{obs} of all functionalized gFETs. It can be observed that the k_{on} of all proteins, apart from OBP14 show a decreasing slope, which is the result of a non-specific binding kinetic. The analysis of k_{on} is a good approach to distinguish between specific and unspecific binding kinetics.

4.6 Eugenol biosensing with protective layers on rGO

In this section the results of gFET biosensing with protective layers are shown. Different protective layers were applied on the rGO surface, such as protein surface-layer and metal oxides. The protection is used to avoid the unspecific binding of the analyte to the rGO surface of the gFET. The biomolecules for sensing are immobilized on top of these additional layers. In table 4.3 all applied protective layers and preparation materials used for adhesion of the layers are listed.

The first measurements carried out with the protective layers on the gFETs surface were cyclic voltammetry and $I_D V_G$ curves to determine the proper function of the gFET.

Protective layer		
layer type	Thickness (nm)	Preparation
Al_2O_3	20	blank rGO
Al Al_2O_3	24	Al seed layer
TiO_2	30	blank rGO
Al TiO_2	34	Al seed layer
Ta_2O_5	20	blank rGO
S-Layer	9	PLL

Table 4.3: Applied protective layer on graphene surface of gFET.

4.6.1 Cyclic voltammetry

Cyclic voltammetry of all metal oxide protective layers was performed to measure the electron transport through the protective layer. Fig. 4.15 shows the measured cyclic voltammetry of six different gFET surfaces.

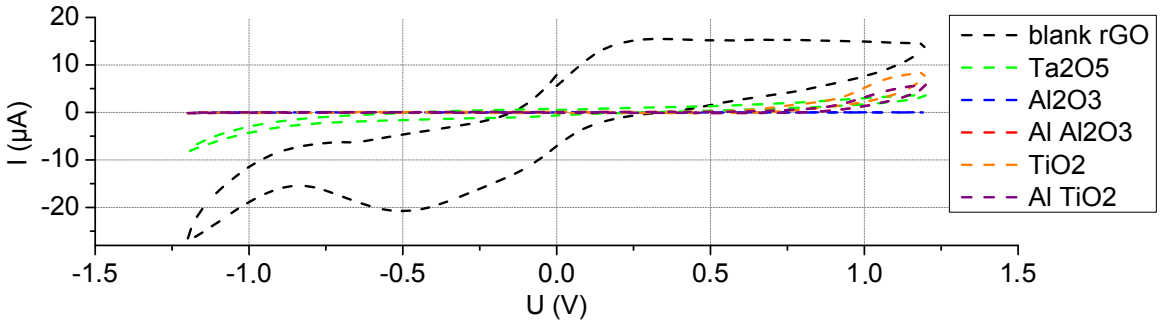

Figure 4.15: Cyclic voltammetry of gFETs with blank rGO surface and metal oxide protective layers. The CV voltage was ramped up from -1.2V to +1.2V and reverse again.

The cyclic voltammetry (CV) for metal oxides shows that if the insulating layer is pinhole free, no electron leakage is possible. Pinholes in passivation layers are associated with nano- or microscopic defects in otherwise completely insulating layers, allowing electron transfer. As reference, CV was also run on the blank rGO gFET, where the current of the redox reaction ranges from -25 μA to 20 μA. The metal oxide layer of Ta_2O_5 was not pinhole free, since the current still ranges from -8 μA to 5 μA, but definitely protects the blank rGO surface, especially in the used voltage range of -700 mV to -400 mV. The TiO_2 with and without aluminium seed layer reaches currents up to 7 μA for positive voltage of the cyclic voltammetry. This is due to the titanium dioxide's semiconducting properties [100], but since this oxide layer has no current in the negative regime, it seems to be pinhole free. The Al_2O_3 protective layer shows the lowest current of all measured oxide layers i.e. the current does not exceed 100 nA with or without an aluminum seed layer. One can therefore assume that it is pinhole free.

It can be concluded that all protective layers reduce the electron leakage to the ionic liquid and therefore all metal oxides are suitable for gFET application. Only the Ta_2O_5 seems to have pinholes in the observed voltage regime, so a current flow from graphene to the analyte solution occurs. The cyclic voltammetry was only carried out on metal oxide layers, because the bacterial cell surface (S-Layer) is not an insulating layer.

4.6.2 I_DV_G of gFET with protective layer

In Fig. 4.16 (a) and (b) the measured I_DV_G hysteresis curves of Al_2O_3 and Ta_2O_5 gFETs are shown. Fig. 4.16 (c) and (d) show the I_DV_G curves of protein s-layer and TiO_2 protective layer. In all measurements linear fits were made to determine the electron mobility of the gFETs. The hysteresis of the I_DV_G curves show different shapes, regarding whether the V_G sweep was performed from negative to positive values or vice versa. The effect is described in the studies of Wang et al. [101], by investigation on the electron trapping in the graphene layer on SiO_2 wafers. The neutral point NP shifts, depending on the V_G sweep direction for 0.3 to 0.4 mV. If V_G starts at a negative voltage, the holes are slowly trapped on the graphene, so the positive potential applied to the graphene surface is higher than just the gate voltage. Therefore the NP is shifted up to the positive regime. For that kind of I_DV_G sweep, the charges stay in the electron traps until the polarity of V_G changes. The shift of the Neutral Point was observed for the Ta_2O_5 coated gFET. It can be said that electron trapping on the graphene surface takes place when using this protective layer. The Al_2O_3 gFET has a negligible neutral point shift, showing that electron trapping is inhibited when this layer is applied on the rGO. The s-layers I_DV_G curve is very similar to the blank rGO gFET except for the fact that the mobility halves for the additional layer on the graphene surface. The I_DV_G curve of the TiO_2 protective layer is not suited for a linear fit and has no clear polarity of hole or electron mobility, so it cannot be used for the present gFET set-up.

Comparison of electron mobilities

The slope of the linear fit of the I_DV_G curve is proportional to the electron mobility, see description in equation (3.1). In Tab. 4.4 the electron mobilities for rGO and all evaluated protective layers are listed. All measured I_DV_G curves and the calculated electron mobilities show that the Al_2O_3 and Ta_2O_5 metal oxide gFETs would be the most appropriate to be used in analytical measurements. The decrease of mobility will result in a decreasing response, but it can be justified with an significant decrease of unspecific bindings. The protein s-layer has half of the electron mobility of rGO and should lead to similar results on detecting specific analytes as already measured on the unprotected gFET. In literature, the calculated maximum mobilities of graphene at room temperature range from 10.000 cm^2/Vs [14] to 26.000 cm^2/Vs [102] or ultra high electron mobilities even up to 200.000 cm^2/Vs [103] of single layer graphene in the presence of an electric field.

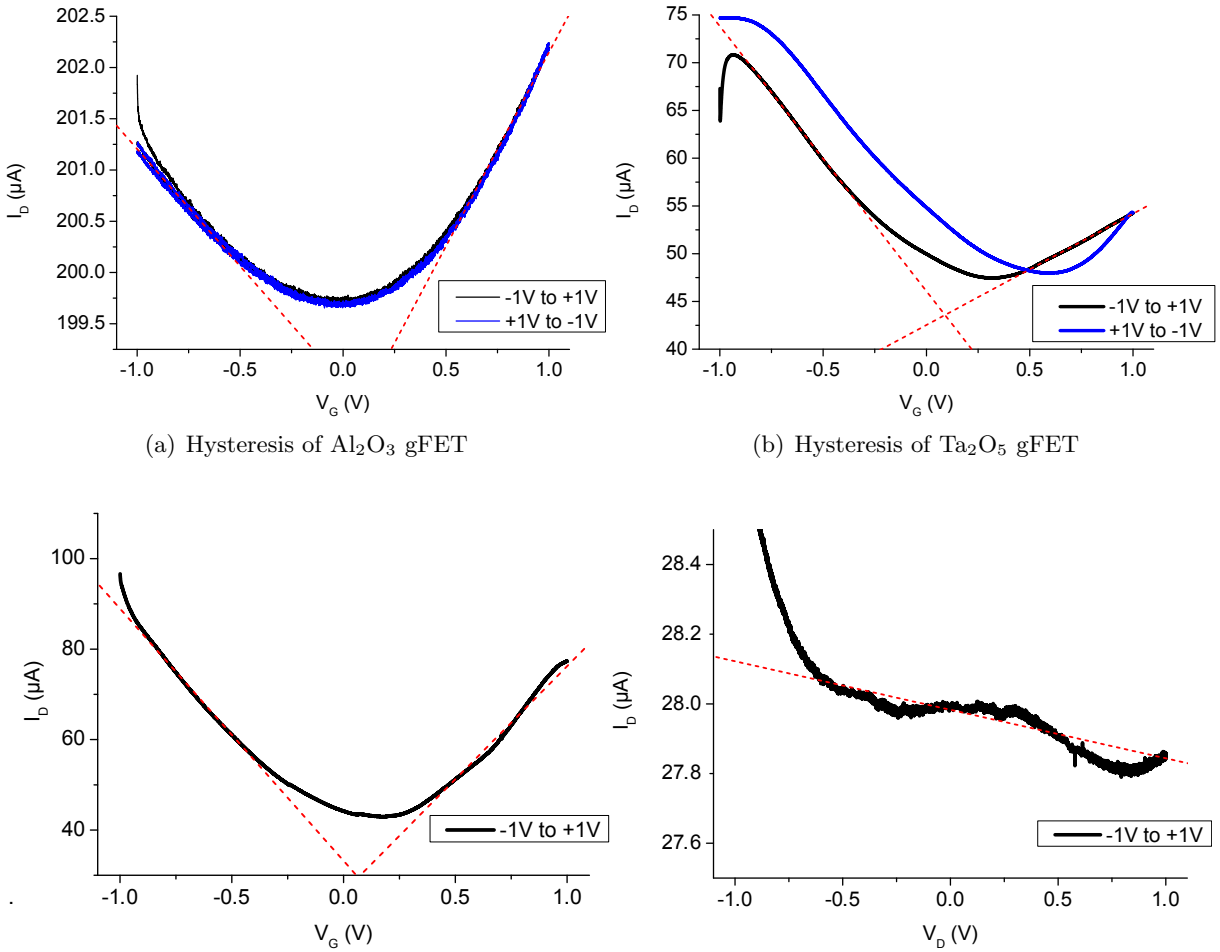

(a) Hysteresis of Al_2O_3 gFET

(b) Hysteresis of Ta_2O_5 gFET

(c) S-layer gFET

(d) TiO_2 gFET

Figure 4.16: Measured $I_D V_G$ curves of gFETs with protective layer on top of the rGO surface. The hysteresis of the drain-source current I_D was measured while the gate voltage V_G ramped up from -1 V to +1 V and back, shown in (a) for Al_2O_3 and in (b) for Ta_2O_5. The $I_D V_G$ curves of an S-layer gFET (c) and a TiO_5 gFET (b) were charactarized from -1 V to +1 V. The red dashed lines are linear fits to determine the electron mobility of the rGO with protective layer.

Mobilities				
gFET surface	Slope m_{lin} (μA/V)	Hole mobility μ_{hole} ($cm^2/(Vs)$)	Slope m_{lin} (μA/V)	Electron mobility $\mu_{electron}$ ($cm^2/(Vs)$)
rGO	-54.6	36.000	68.5	45.660
S-Layer	-55.7	18.500	50.0	16.650
Ta_2O_5	-27.7	4.340	11.7	4.940
Al_2O_3	-2.28	390	3.8	630
Al Al_2O_3	-1.13	160	0.65	110
TiO_2	-0.14	90	-	-
Al TiO_2	-0.033	20	-	-

Table 4.4: Results of hole and electron mobilities for measured gFET surfaces.

4.6.3 Immobilization of proteins on protective layers

Functionalization of a protective layer gFET requires other methods to immobilize proteins than on blank rGO. In this section the results of protein immobilization on metal oxides and protein s-layer are shown and discussed.

4.6.4 Fluorescence analyses of immobilized proteins on metal oxide layer

The immobilization of proteins on the oxide layers was verified by fluorescence microscopy. Fig. 4.17 shows the results of the microscopy at λ_{ex} = 488 nm and λ_{em} = 500 - 550 nm. The images were taken at three different immobilization states: (a) only GPTMS linker, (b) GPMTS-linked protein and (c) protein washed off with pH 2 buffer solution. C*c*O proteins were labelled with fluorescein and immobilized on the metal oxide protective layers to study the applicability of the GPTMS linker.

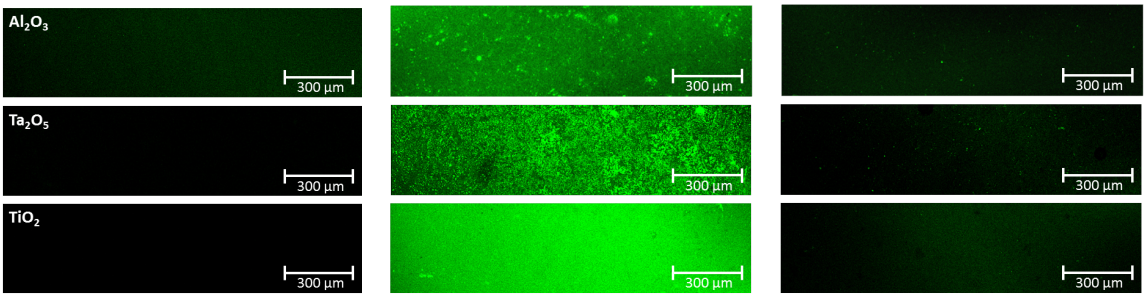

(a) Only GPTMS linker (b) linker and protein (c) linker and protein after pH2 wash

Figure 4.17: Fluorescence microscopy at λ_{ex} = 488 nm and λ_{em} = 500 - 550 nm images of CcO protein immobilized on metal oxide layer. (a) shows the fluorescence of just GPTMS linker on the metal oxide surface. CcO was labelled with fluorescein, linked with GPTMS and the fluorescence is shown in (b). In (c) the protein was removed with pH 2 buffer washing. The immobilization was evaluated on Al_1O_3, Ta_2O_5 and TiO_2

The fluorescence images prove that the immobilization of proteins with GPTMS linker on the metal oxide surface does take place and can be used for functionalization of metal oxide gFETs with OBP14. All three metal oxides show remarkably high fluorescein concentrations after linking C*c*O to GPTMS, with TiO_2 showing the highest intensity i.e. mean gray value of GV_{mean} = 50.5. The gray value of Al_2O_3 is GV_{mean} = 27.5 and of Ta_2O_5 GV_{mean} = 39.5, on the gray scale of 255. After pH 2 buffer washing, no more fluorescence was detected. This could be explained by the loss of either the GPTMS linker or the C*c*O protein florescence label after pH 2 buffer washing.

4.6.5 OBP14 immobilized on protective layer to measure eugenol binding kinetics

Al_2O_3, Ta_2O_5 and s-layer gFETs were functionalized with OBP14 and measured with impedance spectroscopy after evaluation of electron mobilities and insulation. See in Fig. 4.18 (a) the normalized magnitude |Z| of eugenol titration and in (b) the Langmuir, respectively linear fits for the protective layer gFETs of eugenol and BSA titration. The metal oxide gFETs had no

response at 1 Hz, but a maximum Δ |Z| at 68 Hz for the Ta_2O_5 and 200 kHz for Al_2O_3 gFET. The reason for no response in the low frequency regime might be the insulation between graphene and the odorants. Only at frequencies above 50 Hz the capacitive coupling between graphene and the proteins leads to a change in conductivity. For BSA titration the Al_2O_3 gFET had no response in the entire impedance spectrum and the baseline was very stable at all frequencies. The Langmuir fit for eugenol titration on the Al_2O_3 gFET were not performed, because the response did not show proper binding kinetics.

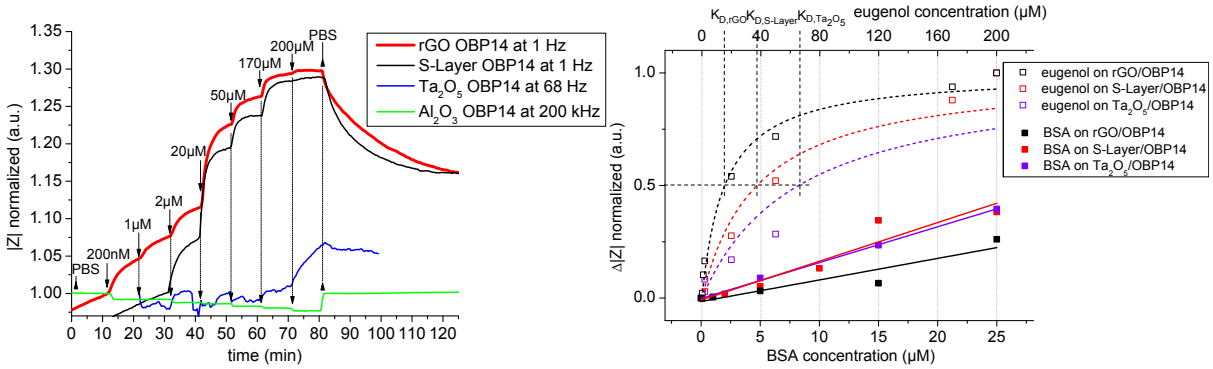

(a) OBP14 immobilized on rGO and on protective layers

(b) Langmuir fit eugenol

Figure 4.18: Titration of eugenol and BSA on functionalized protective layer gFETs. Immobilized OBP14 on rGO, s-layer, Al_2O_3 and Ta_2O_5 surfaces were measured. The normalized magnitude |Z| of specific eugenol bindings on all chips is shown in (a) at 1 Hz for rGO and s-layer gFET, whereas |Z| at 200 kHz for Al_2O_3 and at 68 Hz for Ta_2O_5 is shown. The Langmuir fit of the OBP14 on rGO, Ta_2O_5 and s-layer are shown in (b), with the corresponding unspecific BSA response. At 50% of surface coverage the dissociation constant K_D for the three gFETs are tagged.

The magnitude |Z| of the OBP14 s-layer gFET at 200 μM eugenol is 99.3% of the unprotected OBP14 gFET. The first measured response occurred at a eugenol concentration of 2 μM, meaning, the limit of detection is higher than on the reference gFET. These two negative effects are due to the increasing distance of OBP14 to the rGO surface, that the conformational charge transfer has lower influence to |Z|. In Fig. 4.18 (b) the comparison of binding affinities to unspecific molecules, here protein BSA, were higher than on the rGO/OBP14 gFET. The slopes k_{on} for s-layer and Ta_2O_5 are about 1.7 times steeper than for the unprotected gFET. This might be due to a lower hydrophobicity of protective layers, so the sticky BSA proteins adhere on the surface and increase the magnitude |Z|.

The maximum response Δ |Z| to eugenol of the OBP14 Ta_2O_5 gFET was at 68 Hz, so the gFET was evaluated at this frequency. Even at 68 Hz the Ta_2O_5 gFET had little response magnitude |Z| to different eugenol concentrations and it had drift for concentrations below 50 μM, which made an evaluation impossible. The Langmuir fit of the measured magnitude |Z| can hardly be performed, because the data cannot be accurately interpreted. Consequently, the resulting dissociation constant K_D lacks in precision.

The OBP14 Al_2O_3 had a very stable performance during the impedance spectroscopy. There was no baseline drift and no unspecific response to protein BSA. In Fig. 4.18 (a) the response of the functionalized Al_2O_3 gFET to different eugenol concentrations is shown at a frequency of 200 kHz, because here the maximum response Δ |Z| was measured. The minor change in

magnitude is due to the thickness of 20nm of Al_2O_3, but since the noise and baseline drift of Al_2O_3 gFETs are very low, the SNR is high and the measurement can be evaluated.

Response of eugenol to Al_2O_3 gFET with immobilized OBP14

Fig. 4.19 (a) shows the entire normalized magnitude spectrum at eugenol titration on OBP14 Al_2O_3 gFET from 1 Hz to 500 kHz, where the scale of |Z| is inverted. The 3D demonstration of |Z| illustrates that the response of Al_2O_3 gFETs starts at 10 kHz and the highest Δ |Z| is at 200 kHz. The decrease of magnitude |Z| at 200 kHz for different eugenol concentrations on the OBP14 Al_2O_3 gFET is shown in Fig. 4.19 (b).

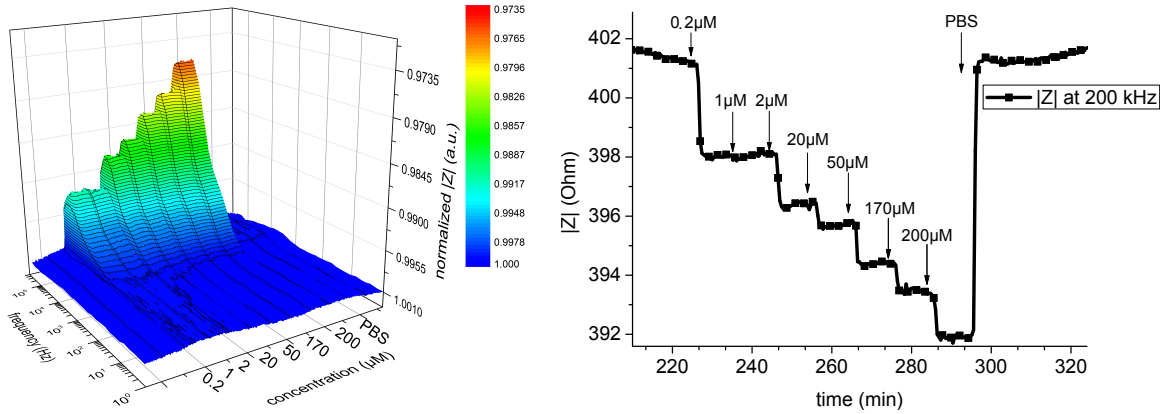

(a) Normalized |Z| spectrum

(b) |Z| at 200 kHz

Figure 4.19: Response |Z| to different eugenol concentrations on gFET with 20 nm Al_2O_3 protective layer. The 3D spectrum of the normalized magnitude |Z| is shown in (a). The response |Z| at 200 kHz is shown in (b).

In previous measurements, an increasing eugenol concentration resulted in increasing magnitude |Z|, while the measurement of Al_2O_3 gFETs result in a decreasing |Z| at higher eugenol concentrations. Furthermore, the maximum Δ |Z| occurred at 200 kHz, whereas OBP14 rGO gFETs had their maximum magnitude change between 1 Hz and 100 Hz.

These results lead to the conclusion, that it was the change in ion concentration in the buffer solution that was actually measured and not the conformational charge re-distribution of ligand binding. To compare the gFET's eugenol response to ion concentration response of Al_2O_3 the impedance spectrum for different PBS buffers was measured and is shown in Fig. 4.20 (a). The magnitude |Z| was normalized to the gFETs response at the lowest ion concentration 21.25 mM in PBS buffer and the scale of the magnitude was inverted for a better illustration. Selected frequencies of this spectrum are shown in Fig. 4.20 (b).

The comparison of Fig. 4.19 (a) and Fig. 4.20 (a) lead to the assumption, that the response to the eugenol concentration is attributable to different ion concentrations in the solution. As already mentioned in Section 4.4, the ion concentration influences the impedance spectroscopy, especially at frequencies above 1 kHz. An exponential fit for the acquired data can be performed, because the magnitude |Z| and phase(Z) are exponentially dependent on different ionic concentrations. The response to the eugenol titration turned out to be a titration with different ion concentrations, accidentally performed because of contamination of a bottle. The Al_2O_3

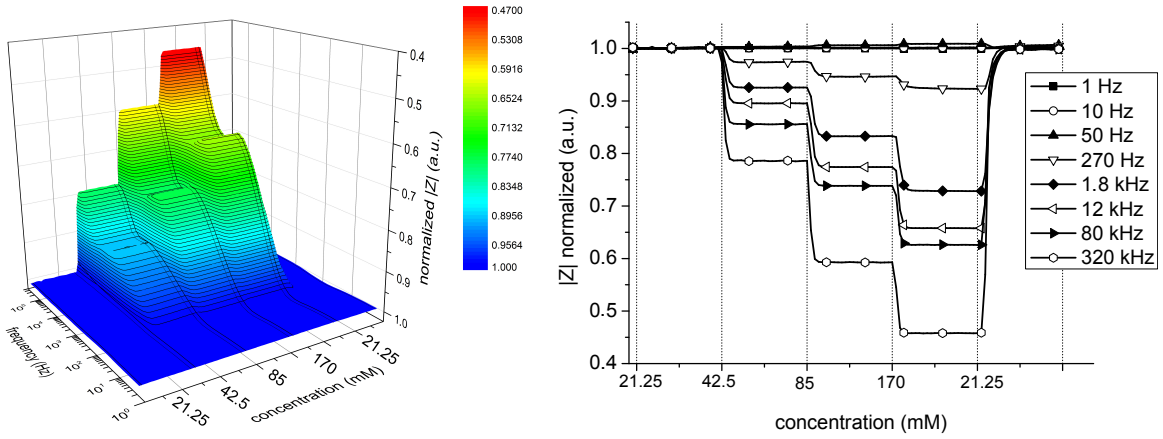

(a) Normalized |Z| spectrum

(b) |Z| different frequecies

Figure 4.20: Response |Z| to different ionic concentrations of PBS buffer on gFET with 20nm Al_2O_3 protective layer. In (a) the three dimensional demonstration of the entire spectrum of the normalized magnitude |Z| is shown. |Z| is normalized to its 21.25mM baseline level at all frequencies. The normalized change of |Z| at different frequencies is shown in (b).

gFET's response was fitted to the ionic strength fitting curve to calculate the ionic strength of the solution. In Fig. 4.21 (b), the calculated ionic concentrations are labeled to the response of the OBP14 Al_2O_3 gFET. The exponential fitting curve was calculated for 200 kHz to compare it with the maximum response of the gFET at eugenol titration.

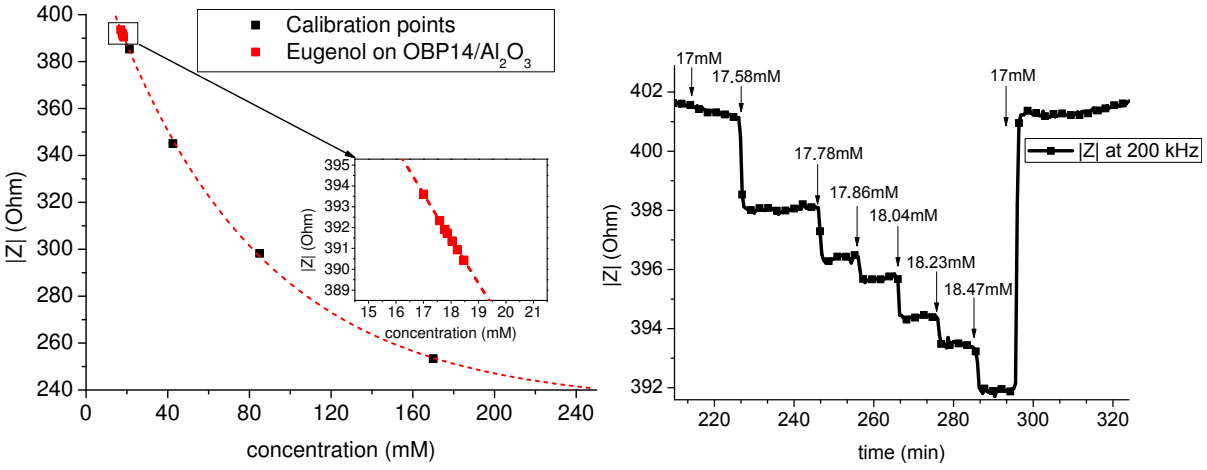

(a) Calibration of |Z| to ionic concentration

(b) Calculated values for ionic concentration

Figure 4.21: The calibration curve for ionic concentration dependency was calculated with an ion concentration measurement on an Al_2O_3 gFET, shown in (a). The measurements of the eugenol titration, which was contaminated with different ion concentrations was fitted on this curve. With the exponential fit it is possible to estimate the ionic concentration of this measurement. The calculated values of the found ionic concentration in the different eugenol solutions were calculated and are shown in (b). This response is the eugenol measurement from Fig. 4.19 (b), but with the calculated values for ionic concentrations.

After investigation of the response of the OBP14 Al_2O_3 gFET to the eugenol titration, it can be said, that the influence of different ionic concentrations may cause wrong interpretations. On the other hand, the gFETs impedance spectroscopy to unknown solutions has the potential to distinguish between protein-ligand interactions in the low frequency regime and

ion concentrations in the solution in the high frequency regime. Considering these conclusions, the measurement of the OPB14 Al_2O_3 gFET, see Fig. 4.19 (b), shows no response to eugenol. The decrease of magnitude |Z| at 200 kHz results from the increase of ion concentrations. The measured ion concentrations stem from the preparation of the eugenol titration.

Probably the 200 μM eugenol stock solution was prepared in a contaminated bottle, where other ions still adhered on the sidewalls. Since there was no specific response of the OBP14 measured, the Al_2O_3 protective layer might shield the charge transfer at binding activities. The capacitive coupling to the aqueous solution at frequencies above 1 kHz lead to an ion concentration related response.

4.6.6 Observed and calculated kinetic parameters for eugenol bindings to proteins

In this section all measured gFETs with immobilized proteins are listed in Tab. 4.5. The measurements were performed as mentioned in Section 4.5 to calculate the kinetics. The dissociation constants K_D were calculated with equation (4.3) from the linear fit of k_{obs}.

Kinetic parameters			
gFET	fitting parameters		calculated parameters
type surface/protein	Slope k_{on} $(M^{-1}s^{-1})$	Intercept k_{off} $(mM^{-1}s^{-1})$	dissociation constant K_D (M)
rGO/-	5.93	3.33	$5.61e^{-3}$
rGO/OBP14	34.97	5.75	$1.64e^{-4}$
S-Layer/OBP14	16.06	6.04	$3.76e^{-4}$
rGO/Anti-BSA	-1.52	2.76	$-1.82e^{-3}$
rGO/Lysozym	-18.86	7.80	$-4.13e^{-4}$
rGO/OBP9A	-23.89	8.48	$-3.54e^{-4}$
rGO/OBP9B	-12.1	5.42	$-4.48e^{-4}$

Table 4.5: Table of kinetic parameters of all measured gFETs.

A small dissociation constant K_D represents high affinity K_A, due to the reciprocal relation in equations (2.6) and (2.7). With the assumption, that the OPB14 has the same affinity on every gFET, the difference in K_D stems from different sensor set-ups. Each preparation method influences the distance of surface-immobilized OPBs to the graphene surface, the mobility of electrons and holes, the hydrophobicity of graphene and the undesired surface reactions of analyte and graphene. The standard measurement of graphene FETs with immobilized OBP14 shows the biggest responses in magnitude |Z| and lead to the lowest values of K_D. The rGO/OBP14 gFETs have the highest sensitivity compared to the other preparation methods, with a lowest detectable concentration of 200 nM. All protective S-layer gFET with OBP14 functionalization have a reduced response to eugenol. Metal oxide protective layers are not showing any specific response to eugenol and no K_D can listed in Tab. 4.5. The results for protective layer are not leading to a significant improvement of the graphene FET, so the application of these layers cannot be suggest in future designs. The reasons for this performance might be the thickness of the protective layers or a damage of the graphene surface during the manufacturing process.

The application of protective layers are done in a special environment, suitable for atomic layer deposition of metal oxides or to attach an S-layer on the graphene surface. An explicit investigation on the surface before and after the treatment has not been done, but it can be said, that the ohmic resistance increased during the manufacturing process. Further investigations have to be done to evaluate possibilities of reducing unspecific response of the gFET biosensor system.

5 Conclusion and Outlook

Some words to the conclusion and outlook in general ...

5.1 Conclusion

Graphene oxide and graphene

The production of graphene in the laboratory at AIT was carried out successfully as demonstrated by SEM images of reduced graphene oxide on silicon substrates. The resulting reduced graphene oxide flakes were were suitable for the development of a field-effect transistor with graphene in the drain-source channel. However, problems did arise with the in-house production of graphene i.e. impurities and high variation of flake size. In the initial tests GO was produced with the modified Hummers method [18]. Highly pure GO produced by Bayreuth University was used subsequently for further investigation on rGO. This GO led to higher yields in gFET production and lower ohmic resistance between drain and source due to higher rGO density in solution.

The reduction process of the insulating material graphene oxide to the required conducting material graphene was carried successfully out using hydrazine, a highly carcinogenic chemical. Alternatives, to replace this method were searched and found in hydriodic acid (HI), which is still toxic, but not carcinogenic.

Biosensor gFET with OPB14

After attaching GO to a silicon wafer and reducing to rGO, gold electrodes were evaporated onto the graphene surface. The geometrical dimension of the drain-source gap, covered with rGO created a biosensing surface to immobilize proteins using linker chemistry. The immobilized

OPB14 should modulate the conductivity of the graphene flakes depending on kinetic reactions with ligands, such as eugenol. This working principle was shown and tunings of this gFET system were performed in order to obtain higher specificity and lower limits of detection.

Impedance spectroscopy set-up

The measurement system for impedance spectroscopy was set up on an available potentiostat, employing several channels to create a measurement system for drain-source impedance measurements on the gFET. The voltage of the gate electrode was controlled by software to perform all sort of characterizations like $I_D V_G$ and $I_D V_D$ curves, recording binding kinetics in real time and measure the impedance spectrum from 1 Hz up to 500 kHz. A system was developed, where two gFETs were measured at the same time, using two channels of the 16-channel potentiostat VMP3, from Bio-Logic SAS.

Performed measurements

The performed measurements covered the characterization of the gFET under different environmental conditions. The analyte concentrations in aqueous solution were always performed in PBS buffer. The changes of pH value and ion concentration of the buffer solution are shown in Section 4.3 and Section 4.4, leading to an electrical equivalent circuit (EEC) for the gFET system. The binding kinetics of OPB14 to eugenol, such as binding affinities and binding rate constants were measured and calculated by employing the Langmuir theory of surface binding events, see Section 4.5.1. This analysis allows the comparison of measurements of different gFET types - investigated within this work - as well as comparison with other measurement techniques. Beside the high sensitivity, compared to the other evaluated variants of the present gFET, the sensor lacks in selectivity. Even with blank rGO gFETs a K_D of 5.61 mM was measured, while there was no functionalization on the surface. The reason for the affinity of graphene itself can be found in the aromatic structure of odorants, discussed in Section 4.5.1. π-π stacking on the graphene surface leads to significant conductivity changes that appear to show a specific binding, discussed in Section 4.5.1.
To avoid the contact of aromatic analytes with graphene, protective layers were applied. The working principle to reduce the unspecific bindings of analytes to graphene with protective layers depends on the applied method. Metal oxide layers insulate graphene from the bulk solution and therefore reduce the influence of π-π stacking of analytes. Another approach is covering the graphene surface with a bacterial cell surface layer, the S-layer. This crystalline surface structure is hydrophobic and should be a spacer between the bulk solution and graphene. The hydrophobic properties of the S-layer prevent the analyte from adhering to the graphene and to produce unspecific signals. The metal oxide surfaces reduced the unspecific bindings of eugenol to graphene, but also insulates the OPBs, so the modulation of the drain-source current I_D due to conformational changes can no longer be measured, shown in Section 4.6.

The functionalization of graphene on metal oxides was controlled by fluorescence measurement, so the immobilization of OBPs on the surface works with the applied molecular linking method, shown in Section 4.6.4. The layers were only few nanometers thick, but the insulating material

avoided significant changes on Ta_2O_5 gFETs and completely damped all response of OPBs on AlO_2 gFETs. Therefore, the K_Ds of metal oxide gFETs cannot be measured and are not listed in Tab. 4.5. Further investigations have be carried out to improve the response on metal oxides. Another protective layer, the S-layer reduces the unspecific signals, but also lowers the response to specific binding events. An improvement of the measurement system cannot be obtained with the applied protective layers.

5.2 Summary and outlook

As a conclusion of the developed biosensor system, utilizing impedance spectroscopy, the odorant sensing of eugenol is possible, including the discrimination of ion concentrations on the aqueous bulk solution. As shown in Section 4.5.1, a specific response to different eugenol concentrations can be measured, while the results of Section 4.6.5 demonstrate, that the calculation of ion concentrations can be performed, due to the impedimetric investigations in frequencies above 1 kHz. Different ion concentrations change the response signal of the functionalized gFET. The resulting ion concentration, obtained by impedance spectroscopy can be used as input for a correction of the response of ligand to OBP binding events. The measurement of analyte concentrations and binding kinetics showed similar results as reported by Larisika et al. [79].

This work can demonstrates an approach of impedance spectroscopy applied on a gFET, employing odorant binding proteins to detect small odorant biomolecules in aqueous solution. The results have no more binding information in frequencies above 100 Hz, therefore the measurement of protein-ligand interaction has not to be performed with impedance spectroscopy. The advantage of the measurements in frequencies above 1 kHz is to calculate the ion concentrations of an unknown aqueous solution. The refinement of the measurement principle is not part of this work and will not be discussed.

Also, protective layers have a high potential to be integrated in biosensors on graphene basis to improve the biosensor platform. Further improvements could be a miniaturization of the solution channel. Microfluidics are an attractive way to decrease the height of the bulk solution channel, increasing the influence of the gate electrode. A multiple gFET system could be established on one silicon chip. Several gFETs on one chip can be used as a detection system with different OBPs immobilized and a negative control. The unspecific influence could be subtracted in a post processing step to get only the specific response of the OBPs. The advantage of more gFETs on one chip would be a decrease of variation between the single devices. The system could be adapted for other biomolecules, such as hormone, toxine or antibody detection. The rising interest in aptamers, short DNA or RNA strands that bind to a specific target, could lead to high specific biosensors, based on graphene FETs.

Bibliography

[1] S.-H. Chan, J.-W. Chen, H.-P. Chen, H.-S. Wei, M.-C. Li, S.-H. Chen, C.-C. Lee, and C.-C. Kuo, "The deviation of growth model for transparent conductive graphene," *Nanoscale research letters*, vol. 9, no. 1, pp. 1–6, 2014.

[2] C. Bushdid, M. O. Magnasco, L. B. Vosshall, and A. Keller, "Humans can discriminate more than 1 trillion olfactory stimuli," *Science*, vol. 343, no. 6177, pp. 1370–1372, 2014.

[3] A. C. Neto, F. Guinea, and N. M. Peres, "Drawing conclusions from graphene," *Physics World*, vol. 19, no. 11, p. 33, 2006.

[4] A. Fasolino, J. Los, and M. I. Katsnelson, "Intrinsic ripples in graphene," *Nature materials*, vol. 6, no. 11, pp. 858–861, 2007.

[5] J. C. Meyer, A. K. Geim, M. Katsnelson, K. Novoselov, T. Booth, and S. Roth, "The structure of suspended graphene sheets," *Nature*, vol. 446, no. 7131, pp. 60–63, 2007.

[6] K. S. Novoselov, "Nobel Lecture: Graphene: Materials in the Flatland," *Reviews of Modern Physics*, vol. 83, no. 3, pp. 837–849, 2011.

[7] C. Lee, X. Wei, J. W. Kysar, and J. Hone, "Measurement of the Elastic Properties and Intrinsic Strength of Monolayer Graphene," *Science*, vol. 321, no. 5887, pp. 385–388, Jul. 2008. [Online]. Available: http://dx.doi.org/10.1126/science.1157996

[8] G. M. Rutter, S. Jung, N. N. Klimov, D. B. Newell, N. B. Zhitenev, and J. A. Stroscio, "Microscopic polarization in bilayer graphene," *Nature Physics*, vol. 7, no. 8, pp. 649–655, 2011.

[9] A. Inaba, K. Yoo, Y. Takei, K. Matsumoto, and I. Shimoyama, "Ammonia gas sensing using a graphene field-effect transistor gated by ionic liquid," *Sensors and Actuators, B: Chemical*, vol. 195, pp. 15–21, 2014. [Online]. Available: http://dx.doi.org/10.1016/j.snb.2013.12.118

[10] A. Geim and K. Novoselov, "The rise of graphene." *Nat. Mater.*, pp. 183–191, 2007.

[11] P. R. Wallace, "The band theory of graphite," *Physical Review*, vol. 71, no. 9, pp. 622–634, 1947.

[12] A. H. Castro Neto, F. Guinea, N. M. R. Peres, K. S. Novoselov, and A. K. Geim, "The electronic properties of graphene," *Rev. Mod. Phys.*, vol. 81, pp. 109–162, Jan 2009. [Online]. Available: http://link.aps.org/doi/10.1103/RevModPhys.81.109

[13] K. Novoselov, A. K. Geim, S. Morozov, D. Jiang, M. Katsnelson, I. Grigorieva, S. Dubonos, and A. Firsov, "Two-dimensional gas of massless dirac fermions in graphene," *nature*, vol. 438, no. 7065, pp. 197–200, 2005.

[14] K. S. Novoselov, A. K. Geim, S. Morozov, D. Jiang, Y. Zhang, S. Dubonos, , I. Grigorieva, and A. Firsov, "Electric field effect in atomically thin carbon films," *science*, vol. 306, no. 5696, pp. 666–669, 2004.

[15] X. Li, W. Cai, J. An, S. Kim, J. Nah, D. Yang, R. Piner, A. Velamakanni, I. Jung, E. Tutuc *et al.*, "Large-area synthesis of high-quality and uniform graphene films on copper foils," *Science*, vol. 324, no. 5932, pp. 1312–1314, 2009.

[16] B. C. Brodie, "On the atomic weight of graphite," *Philosophical Transactions of the Royal Society of London*, pp. 249–259, 1859.

[17] W. S. Hummers Jr and R. E. Offeman, "Preparation of graphitic oxide," *Journal of the American Chemical Society*, vol. 80, no. 6, pp. 1339–1339, 1958.

[18] M. Larisika, J. Huang, A. Tok, W. Knoll, and C. Nowak, "An improved synthesis route to graphene for molecular sensor applications," *Materials Chemistry and Physics*, vol. 136, no. 2, pp. 304–308, 2012.

[19] M. J. McAllister, J.-L. Li, D. H. Adamson, H. C. Schniepp, A. A. Abdala, J. Liu, M. Herrera-Alonso, D. L. Milius, R. Car, R. K. Prud'homme *et al.*, "Single sheet functionalized graphene by oxidation and thermal expansion of graphite," *Chemistry of Materials*, vol. 19, no. 18, pp. 4396–4404, 2007.

[20] H. C. Schniepp, J.-L. Li, M. J. McAllister, H. Sai, M. Herrera-Alonso, D. H. Adamson, R. K. Prud'homme, R. Car, D. A. Saville, and I. A. Aksay, "Functionalized single graphene sheets derived from splitting graphite oxide," *The Journal of Physical Chemistry B*, vol. 110, no. 17, pp. 8535–8539, 2006.

[21] X. Li, G. Zhang, X. Bai, X. Sun, X. Wang, E. Wang, and H. Dai, "Highly conducting graphene sheets and langmuir–blodgett films," *Nature nanotechnology*, vol. 3, no. 9, pp. 538–542, 2008.

[22] Y. Zhu, S. Murali, M. D. Stoller, A. Velamakanni, R. D. Piner, and R. S. Ruoff, "Microwave assisted exfoliation and reduction of graphite oxide for ultracapacitors," *Carbon*, vol. 48, no. 7, pp. 2118–2122, 2010.

[23] Y. Matsumoto, M. Koinuma, S. Y. Kim, Y. Watanabe, T. Taniguchi, K. Hatakeyama, H. Tateishi, and S. Ida, "Simple photoreduction of graphene oxide nanosheet under mild conditions," *ACS applied materials & interfaces*, vol. 2, no. 12, pp. 3461–3466, 2010.

[24] V. C. Tung, M. J. Allen, Y. Yang, and R. B. Kaner, "High-throughput solution processing of large-scale graphene," *Nature nanotechnology*, vol. 4, no. 1, pp. 25–29, 2009.

[25] S. Stankovich, D. A. Dikin, G. H. Dommett, K. M. Kohlhaas, E. J. Zimney, E. A. Stach, R. D. Piner, S. T. Nguyen, and R. S. Ruoff, "Graphene-based composite materials," *Nature*, vol. 442, no. 7100, pp. 282–286, 2006.

[26] J. Zhang, H. Yang, G. Shen, P. Cheng, J. Zhang, and S. Guo, "Reduction of graphene oxide via l-ascorbic acid," *Chemical Communications*, vol. 46, no. 7, pp. 1112–1114, 2010.

[27] S. Pei, J. Zhao, J. Du, W. Ren, and H.-M. Cheng, "Direct reduction of graphene oxide films into highly conductive and flexible graphene films by hydrohalic acids," *Carbon*, vol. 48, no. 15, pp. 4466–4474, 2010.

[28] M. Reisch, *Halbleiter-Bauelemente*. Springer Berlin, 2005.

[29] H. Pfleiderer and W. Kusian, "Ambipolar field-effect transistor," *Solid-state electronics*, vol. 29, no. 3, pp. 317–319, 1986.

[30] J. Millman and C. C. Halkias, *Electronic devices and circuits*. McGraw-Hill, 1967.

[31] D. Neamen, *Electronic Circuit Analysis and Design*, ser. Electronic Circuit Analysis and Design. McGraw-Hill, 2001, no. 1.

[32] C. D. Dimitrakopoulos and P. R. Malenfant, "Organic thin film transistors for large area electronics," *Advanced Materials*, vol. 14, no. 2, p. 99, 2002.

[33] G. Horowitz *et al.*, "Organic field-effect transistors," *Advanced Materials*, vol. 10, no. 5, pp. 365–377, 1998.

[34] I. Meric, M. Y. Han, A. F. Young, B. Ozyilmaz, P. Kim, and K. L. Shepard, "Current saturation in zero-bandgap, top-gated graphene field-effect transistors," *Nature nanotechnology*, vol. 3, no. 11, pp. 654–659, 2008.

[35] M. C. Lemme, T. J. Echtermeyer, M. Baus, and H. Kurz, "A graphene field-effect device," *arXiv preprint cond-mat/0703208*, 2007.

[36] R. Martel, T. Schmidt, H. Shea, T. Hertel, and P. Avouris, "Single-and multi-wall carbon nanotube field-effect transistors," *Applied Physics Letters*, vol. 73, no. 17, pp. 2447–2449, 1998.

[37] A. Javey, J. Guo, Q. Wang, M. Lundstrom, and H. Dai, "Ballistic carbon nanotube field-effect transistors," *nature*, vol. 424, no. 6949, pp. 654–657, 2003.

[38] O. Wunnicke, "Gate capacitance of back-gated nanowire field-effect transistors," *Applied Physics Letters*, vol. 89, no. 8, p. 083102, 2006.

[39] S. Roth and D. Carroll, *One-dimensional metals: conjugated polymers, organic crystals, carbon nanotubes*. John Wiley & Sons, 2006.

[40] A. Matsumoto and Y. Miyahara, "Current and emerging challenges of field effect transistor based bio-sensing," *Nanoscale*, vol. 5, no. 22, pp. 10 702–10 718, 2013.

[41] P. Bergveld, "Development of an ion-sensitive solid-state device for neurophysiological measurements," *IEEE Transactions on Biomedical Engineering*, vol. 1, no. BME-17, pp. 70–71, 1970.

[42] J. Janata and S. D. Moss, "Chemically sensitive field-effect transistors." *Biomedical engineering*, vol. 11, no. 7, p. 241, 1976.

[43] M. J. Schöning and A. Poghossian, "Recent advances in biologically sensitive field-effect transistors (biofets)," *Analyst*, vol. 127, no. 9, pp. 1137–1151, 2002.

[44] S. Caras and J. Janata, "Field effect transistor sensitive to penicillin," *Analytical Chemistry*, vol. 52, no. 12, pp. 1935–1937, 1980.

[45] R. B. M. Schasfoort, R. Kooyman, P. Bergveld, and J. Greve, "A new approach to immunofet operation," *Biosensors and Bioelectronics*, vol. 5, no. 2, pp. 103–124, 1990.

[46] P. Zhao, J. Chauhan, and J. Guo, "Computational study of tunneling transistor based on graphene nanoribbon," *Nano letters*, vol. 9, no. 2, pp. 684–688, 2009.

[47] N. Harada, K. Yagi, S. Sato, and N. Yokoyama, "A polarity-controllable graphene inverter," *Applied Physics Letters*, vol. 96, no. 1, p. 012102, 2010.

[48] J. Noh, K. E. Chang, C. H. Shim, S. Kim, and B. H. Lee, *Performance prospect of graphene barristor with high on-off ratio.* Silicon Nanoelectronics Workshop (SNW), 2014 IEEE, June 2014.

[49] A. D. McNaught, *IUPAC Compendium of Chemical Terminology: The Gold Book.* International Union of Pure and Applied Chemistry, 2005.

[50] M. Pumera, "Graphene in biosensing," *Materials today*, vol. 14, no. 7, pp. 308–315, 2011.

[51] A. Facchetti, M.-H. Yoon, and T. J. Marks, "Gate dielectrics for organic field-effect transistors: new opportunities for organic electronics," *Advanced Materials*, vol. 17, no. 14, pp. 1705–1725, 2005.

[52] B. Van Zeghbroeck, "Principles of semiconductor devices," *Colarado University*, 2004.

[53] G. Higashi and C. Fleming, "Sequential surface chemical reaction limited growth of high quality al2o3 dielectrics," *Applied Physics Letters*, vol. 55, no. 19, pp. 1963–1965, 1989.

[54] S. K. Kim, W.-D. Kim, K.-M. Kim, C. S. Hwang, and J. Jeong, "High dielectric constant tio2 thin films on a ru electrode grown at 250 c by atomic-layer deposition," *Applied physics letters*, vol. 85, no. 18, pp. 4112–4114, 2004.

[55] J. Lin, N. Masaaki, A. Tsukune, and M. Yamada, "Ta2o5 thin films with exceptionally high dielectric constant," *Applied physics letters*, vol. 74, p. 2370, 1999.

[56] C.-C. Cheng, C.-H. Chien, G.-L. Luo, J.-C. Liu, C.-C. Kei, D.-R. Liu, C.-N. Hsiao, C.-H. Yang, and C.-Y. Chang, "Characteristics of atomic-layer-deposited al2o3 high-k dielectric films grown on ge substrates," *Journal of The Electrochemical Society*, vol. 155, no. 10, pp. G203–G208, 2008.

[57] B. Liu, P.-J. J. Huang, X. Zhang, F. Wang, R. Pautler, A. C.-F. Ip, and J. Liu, "Parts-per-million of polyethylene glycol as a non-interfering blocking agent for homogeneous biosensor development," *Analytical chemistry*, vol. 85, no. 21, pp. 10 045–10 050, 2013.

[58] Y. Xiao and S. N. Isaacs, "Enzyme-linked immunosorbent assay (elisa) and blocking with bovine serum albumin (bsa)—not all bsas are alike," *Journal of immunological methods*, vol. 384, no. 1, pp. 148–151, 2012.

[59] H.-J. Butt, K. Graf, and M. Kappl, *Physics and chemistry of interfaces*. John Wiley & Sons, 2006.

[60] M. Yang, H. C. Yau, and H. L. Chan, "Adsorption kinetics and ligand-binding properties of thiol-modified double-stranded dna on a gold surface," *Langmuir*, vol. 14, no. 21, pp. 6121–6129, 1998.

[61] D. J. O'Shannessy and D. J. Winzor, "Interpretation of deviations from pseudo-first-order kinetic behavior in the characterization of ligand binding by biosensor technology," *Analytical biochemistry*, vol. 236, no. 2, pp. 275–283, 1996.

[62] I. Langmuir, "The constitution and fundamental properties of solids and liquids. part i. solids." *Journal of the American Chemical Society*, vol. 38, no. 11, pp. 2221–2295, 1916.

[63] R. B. Schasfoort and A. J. Tudos, *Handbook of surface plasmon resonance*. Royal Society of Chemistry, 2008.

[64] P. Pelosi, "Odorant-binding proteins," *Critical reviews in biochemistry and molecular biology*, vol. 29, no. 3, pp. 199–228, 1994.

[65] L. Briand, C. Nespoulous, V. Perez, J.-J. Rémy, J.-C. Huet, and J.-C. Pernollet, "Ligand-binding properties and structural characterization of a novel rat odorant-binding protein variant," *European Journal of Biochemistry*, vol. 267, no. 10, pp. 3079–3089, 2000.

[66] M. Tegoni, P. Pelosi, F. Vincent, S. Spinelli, V. Campanacci, S. Grolli, R. Ramoni, and C. Cambillau, "Mammalian odorant binding proteins," *Biochimica et Biophysica Acta (BBA)-Protein Structure and Molecular Enzymology*, vol. 1482, no. 1, pp. 229–240, 2000.

[67] P. Pelosi and R. Maida, "Odorant-binding proteins in insects," *Comparative Biochemistry and Physiology Part B: Biochemistry and Molecular Biology*, vol. 111, no. 3, pp. 503–514, 1995.

[68] Y. Hou, N. Jaffrezic-Renault, C. Martelet, A. Zhang, J. Minic-Vidic, T. Gorojankina, M.-A. Persuy, E. Pajot-Augy, R. Salesse, V. Akimov *et al.*, "A novel detection strategy for odorant molecules based on controlled bioengineering of rat olfactory receptor i7," *Biosensors and Bioelectronics*, vol. 22, no. 7, pp. 1550–1555, 2007.

[69] J. Krieger, E. von Nickisch-Rosenegk, M. Mameli, P. Pelosi, and H. Breer, "Binding proteins from the antennae of bombyx mori," *Insect biochemistry and molecular biology*, vol. 26, no. 3, pp. 297–307, 1996.

[70] A. Schwaighofer, C. Kotlowski, C. Araman, N. Chu, R. Mastrogiacomo, C. Becker, P. Pelosi, W. Knoll, M. Larisika, and C. Nowak, "Honey bee odorant-binding protein 14: effects on thermal stability upon odorant binding revealed by ft-ir spectroscopy and cd measurements," *European Biophysics Journal*, vol. 43, no. 2-3, pp. 105–112, 2014.

[71] I. Iovinella, F. R. Dani, A. Niccolini, S. Sagona, E. Michelucci, A. Gazzano, S. Turillazzi, A. Felicioli, and P. Pelosi, "Differential expression of odorant-binding proteins in the mandibular glands of the honey bee according to caste and age," *Journal of proteome research*, vol. 10, no. 8, pp. 3439–3449, 2011.

[72] P. Pelosi, "Odorant-binding proteins: structural aspects." *Annals of the New York Academy of Sciences*, vol. 855, no. September 2015, pp. 281–293, 1998.

[73] S. Spinelli, A. Lagarde, I. Iovinella, P. Legrand, M. Tegoni, P. Pelosi, and C. Cambillau, "Crystal structure of apis mellifera obp14, a c-minus odorant-binding protein, and its complexes with odorant molecules," *Insect Biochemistry and Molecular Biology*, vol. 42, no. 1, pp. 41–50, 2012, cited By 0.

[74] E. F. Pettersen, T. D. Goddard, C. C. Huang, G. S. Couch, D. M. Greenblatt, E. C. Meng, and T. E. Ferrin, "Ucsf chimera—a visualization system for exploratory research and analysis," *Journal of computational chemistry*, vol. 25, no. 13, pp. 1605–1612, 2004.

[75] S. H. Lee, H. J. Ko, and T. H. Park, "Real-time monitoring of odorant-induced cellular reactions using surface plasmon resonance," *Biosensors and Bioelectronics*, vol. 25, no. 1, pp. 55–60, 2009.

[76] I. Benilova, V. I. Chegel, Y. V. Ushenin, J. Vidic, A. P. Soldatkin, C. Martelet, E. Pajot, and N. Jaffrezic-Renault, "Stimulation of human olfactory receptor 17-40 with odorants probed by surface plasmon resonance," *European Biophysics Journal*, vol. 37, no. 6, pp. 807–814, 2008.

[77] S. Paolini, F. Tanfani, C. Fini, E. Bertoli, and P. Pelosi, "Porcine odorant-binding protein: structural stability and ligand affinities measured by fourier-transform infrared spectroscopy and fluorescence spectroscopy," *Biochimica et Biophysica Acta (BBA)-Protein Structure and Molecular Enzymology*, vol. 1431, no. 1, pp. 179–188, 1999.

[78] N. Kasai, I. Sugimoto, M. Nakamura, and T. Katoh, "Odorant detection capability of qcr sensors coated with plasma deposited organic films," *Biosensors and Bioelectronics*, vol. 14, no. 6, pp. 533–539, 1999.

[79] M. Larisika, C. Kotlowski, C. Steininger, R. Mastrogiacomo, P. Pelosi, S. Schütz, S. Peteu, C. Kleber, C. Reiner-Rozman, C. Nowak, and W. Knoll, "Electronic olfactory sensor based on a. mellifera odorant-binding protein 14 on a reduced graphene oxide field-effect transistor," *Angewandte Chemie - International Edition*, 2015, cited By 0; Article in Press.

[80] V. F. Lvovich, *Impedance spectroscopy: applications to electrochemical and dielectric phenomena*. John Wiley & Sons, 2012.

[81] R. Lanche, V. Pachauri, D. Koppenhöfer, P. Wagner, and S. Ingebrandt, "Reduced graphene oxide-based sensing platform for electric cell-substrate impedance sensing," *Physica Status Solidi (A) Applications and Materials Science*, vol. 211, no. 6, pp. 1404–1409, 2014.

[82] M. C. Rodriguez, A.-N. Kawde, and J. Wang, "Aptamer biosensor for label-free impedance spectroscopy detection of proteins based on recognition-induced switching of the surface charge," *Chemical communications*, no. 34, pp. 4267–4269, 2005.

[83] F. Patolsky, M. Zayats, E. Katz, and I. Willner, "Precipitation of an insoluble product on enzyme monolayer electrodes for biosensor applications: characterization by faradaic impedance spectroscopy, cyclic voltammetry, and microgravimetric quartz crystal microbalance analyses," *Analytical chemistry*, vol. 71, no. 15, pp. 3171–3180, 1999.

[84] H. Qi, C. Wang, and N. Cheng, "Label-free electrochemical impedance spectroscopy biosensor for the determination of human immunoglobulin g," *Microchimica acta*, vol. 170, no. 1-2, pp. 33–38, 2010.

[85] M. Quirk and J. Serda, *Semiconductor Manufacturing Technology*. Prentice Hall, 2001.

[86] U. B. Sleytr, B. Schuster, E.-M. Egelseer, and D. Pum, "S-layers: principles and applications," *FEMS microbiology reviews*, vol. 38, no. 5, pp. 823–864, 2014.

[87] K. Kirchberg, H. Michel, and U. Alexiev, "Exploring the entrance of proton pathways in cytochrome c oxidase from paracoccus denitrificans: Surface charge, buffer capacity and redox-dependent polarity changes at the internal surface," *Biochimica et Biophysica Acta (BBA)-Bioenergetics*, vol. 1827, no. 3, pp. 276–284, 2013.

[88] C. Rozman, "Konstruktion und optimierung eines auf graphen basierenden feld-effekt-transistor-devices," Ph.D. dissertation, uniwien, 2013.

[89] A. Villares, G. Pera, I. Giner, P. Cea, M. C. López, and S. Martín, "The use of cyclic voltammetry to probe the passivation of electrode surfaces by well-ordered self-assembly and langmuir–blodgett films. an advanced undergraduate laboratory experiment in surface science and nanomaterials chemistry," *Journal of chemical education*, vol. 86, no. 6, p. 723, 2009.

[90] C. Rost-Bietsch, *Ambipolar and light-emitting organic field-effect transistors*. Cuvillier Verlag, 2005.

[91] P. Blake, E. Hill, A. C. Neto, K. Novoselov, D. Jiang, R. Yang, T. Booth, and A. Geim, "Making graphene visible," *Applied Physics Letters*, vol. 91, no. 6, p. 063124, 2007.

[92] Y. Zhou, X. T. Zu, F. Gao, H. Lv, and H. Xiao, "Adsorption-induced magnetic properties and metallic behavior of graphene," *Applied Physics Letters*, vol. 95, no. 12, p. 123119, 2009.

[93] R. Misra, M. McCarthy, and A. F. Hebard, "Electric field gating with ionic liquids," *Applied physics letters*, vol. 90, no. 5, p. 052905, 2007.

[94] E. Uesugi, H. Goto, R. Eguchi, A. Fujiwara, and Y. Kubozono, "Electric double-layer capacitance between an ionic liquid and few-layer graphene," *Scientific reports*, vol. 3, 2013.

[95] R. I. Masel, *Principles of adsorption and reaction on solid surfaces*. John Wiley & Sons, 1996, vol. 3.

[96] A. Demin and A. Melenevsky, "Bi-langmuir isotherms' applicability for description of interaction of ion-exchange sorbents with protein mixtures," *Journal of chromatographic science*, vol. 44, no. 4, pp. 181–186, 2006.

[97] D. Graham and M. Phillips, "Proteins at liquid interfaces: Ii. adsorption isotherms," *Journal of Colloid and Interface Science*, vol. 70, no. 3, pp. 415–426, 1979.

[98] S. Spinelli, A. Lagarde, I. Iovinella, P. Legrand, M. Tegoni, P. Pelosi, and C. Cambillau, "Crystal structure of apis mellifera obp14, a c-minus odorant-binding protein, and its complexes with odorant molecules," *Insect biochemistry and molecular biology*, vol. 42, no. 1, pp. 41–50, 2012.

[99] J. Bjoerk, F. Hanke, C.-A. Palma, P. Samori, M. Cecchini, and M. Persson, "Adsorption of aromatic and anti-aromatic systems on graphene through π-π stacking," *The Journal of Physical Chemistry Letters*, vol. 1, no. 23, pp. 3407–3412, 2010.

[100] R. G. Breckenridge and W. R. Hosler, "Electrical properties of titanium dioxide semiconductors," *Physical Review*, vol. 91, no. 4, p. 793, 1953.

[101] H. Wang, Y. Wu, C. Cong, J. Shang, and T. Yu, "Hysteresis of electronic transport in graphene transistors," *ACS nano*, vol. 4, no. 12, pp. 7221–7228, 2010.

[102] A. Akturk and N. Goldsman, "Electron transport and full-band electron-phonon interactions in graphene," *Journal of Applied Physics*, vol. 103, no. 5, p. 053702, 2008.

[103] K. I. Bolotin, K. Sikes, Z. Jiang, M. Klima, G. Fudenberg, J. Hone, P. Kim, and H. Stormer, "Ultrahigh electron mobility in suspended graphene," *Solid State Communications*, vol. 146, no. 9, pp. 351–355, 2008.